DEVELOPMENT OF HIGH-THROUGHPUT TABLETOP INSTRUMENTATION AND OPTICAL-DIAGNOSTICS TO EXPLORE SUPERSONIC AND HYPERSONIC PHENOMENA

BY

SHIVASHREE SHIVAMADE GOWDA

THESIS

Submitted in partial fulfillment of the requirements
for the degree of Master of Science in Aerospace Engineering
in the Graduate College of the
University of Illinois Urbana-Champaign, 2024

Urbana, Illinois

Advisors:

Professor Dana Dlott
Assistant Professor Francesco Panerai

ABSTRACT

This study proposes the development of tabletop experimental setup and imaging diagnostics to study the flow physics of hypersonic vehicle and to characterize the damage behavior of high-speed impacts. In this work, by modifying the instrumentation of laser-launched flyer setup used extensively to shock compress energetic samples, we generate shockwaves in gas by driving the metal foils to hypersonic velocities. The proposed setup is capable of tailoring shockwaves in various gaseous mediums by punching out foils of different metals as flyers over a range of velocities (1-7 km/s) in environments of choice. A key aspect of our instrumentation is the development of orthogonal line of sight diagnostics to study shock wave structure in-line and perpendicular to the direction of shock transit. This work focuses primarily on the development of flow field imaging using high-speed Shadowgraph and Schlieren imaging over other diagnostics. Additionally, a necessary level of insight can be attained within the framework of the numerical model to facilitate the interpretation of shockwaves and associated flow fields. In future, the setup will be extended to study high-speed impacts involving debris such as micro-meteoroids and dust particles with hypersonic vehicles and space stations for the development of shielding materials, and the interaction of hypersonic flow fields with micron-sized fuel droplets dripped by a custom-built droplet generator to study detonation wave propagation and interactions with aerosolized fuel droplets. In this work, results of high-speed impact test, the details of the instrumentation and preliminary imaging data will be presented.

To my family & friends.

TABLE OF CONTENTS

CHAPTER 1: STUDYING SUPERSONIC AND HYPERSONIC PHENOMENA

1.1 THE CHALLENGES IN HYPERSONIC RESEARCH

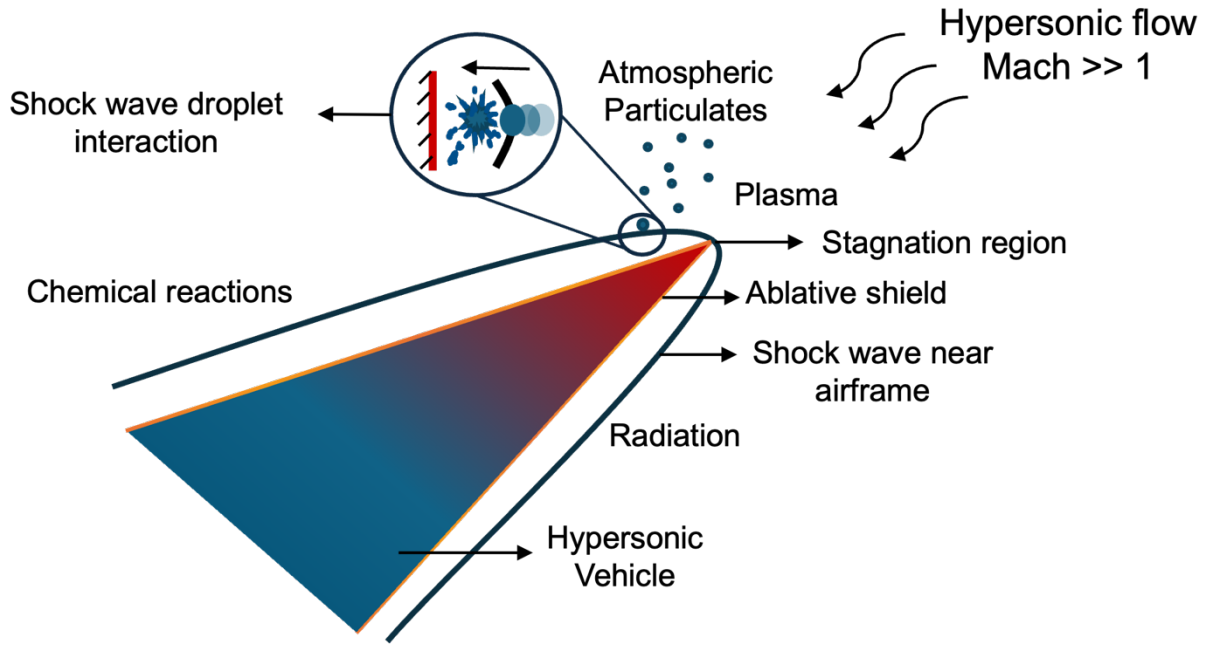

Fig 1.1. Schematic of hypersonic vehicle in a non-equilibrium flow-field

During a high-speed flight, the flow-field/gas environment around the hypersonic vehicles (shown in Fig 1.1) influence thermomechanical loads on the system due to the vehicle's high velocity compared to the speed of sound. In most of the hypersonic applications namely, hypersonic cruise missiles and aircrafts, re-entry vehicles, and interceptor missiles, the velocities are within the range 1.5 - 12 km/s. At these velocities, the vehicles carry extremely high kinetic energy which is transformed to thermal energy due to viscous dissipation, thin shock and entropy layers, shock wave interactions and more. The thermal energy transformation influences high rates of aerodynamic heating and high-temperature flow field including plasma formation at the nose region, radiative heating, and chemically reacting airflows including ablation if the vehicle is protected by an ablative shield, as shown in Fig 1.1.

The challenges of research in hypersonic flight involve the characterization of the flow-field and the high-temperature materials required to progress towards application. Several highly expensive and laborious wind tunnel experiments along with numerical simulations are developed in the past decade to optimize aerodynamic designs and composite materials to withstand the thermal load for specific missions. The material research, in particular, involves a pipeline of extensive laboratory scale development and slow large-scale testing to build promising heatshield/ablative materials. However, for the initial explorative studies of the material behavior at hypersonic speed, a tabletop instrumentation such as laser-driven flyer technique would be really useful given its robustness and high-throughput testing capability.

1.2 SIMULATING HYPERSONIC PHENOMENA IN BENCHTOP EXPERIMENTATION

This dissertation presents an experimental setup capable of simulating hypersonic phenomena of interest described earlier using the well-known and established laser-driven flyer technique. Through this high-throughput benchtop instrumentation we can launch a foil disk (also known as "Flyer") of a variety of metals with different thicknesses (10-200 μm) and diameters (0.5-1.5 mm) from supersonic to hypersonic velocities. Based on the design of experiments these laser-launched flyers are invaluable in studying key aspects of application-oriented research as well as fundamental science.

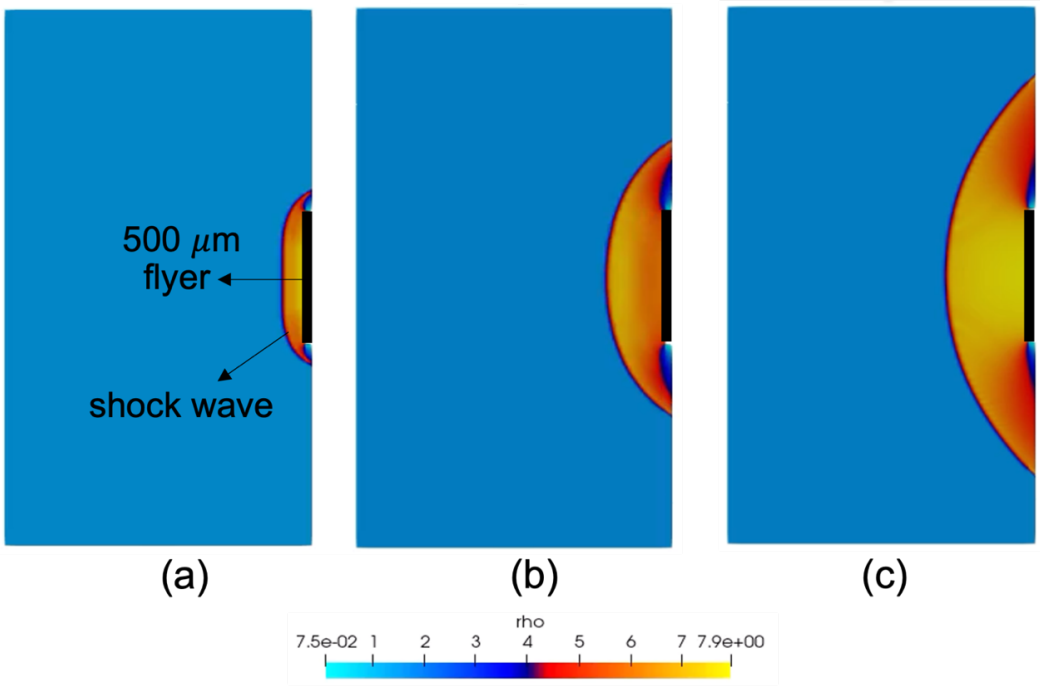

Fig 1.2. Numerical simulation of density contours around a 2D flyer travelling with a velocity of 2 km/s

As an initial characterization, the proposed instrumentation's flyer trajectory was modeled using a numerical solver. Through simulation of flyer launch using a numerical model, it was possible to visualize the flow-field around the flyer and the flyer-driven shock wave, and analyze pressure, density, velocity, and temperature distributions around the flyer upstream. In this work, only the density contours are pursued due to its relevancy with the imaging techniques that focus on capturing the density gradient around the flyer.

Fig 1.2 illustrates the density contour of a 2D flyer of diameter 500 μm numerically modeled to operate at a velocity of 2 km/s under STP conditions using an unsteady two-dimensional density-based coupled Reynolds Averaged Navier-Stokes (RANS) equations on OpenFOAM solver. In this modelling work, the flyer was assumed to remain flat and mechanically unyielding (seen as

the dark rectangle on the right side). From Fig 1.2a, 1.2b, and 1.2c, the evolution of flyer-driven bow shock wave and the increase in gas density in front of the flyer surface can be observed.

As the solver used in this numerical study are based on equilibrium phenomena, it is not possible to comment on the accuracy of the magnitude of the density obtained. However, it does give an overview of the flow distribution around the flyer which is in close approximation to the theory.

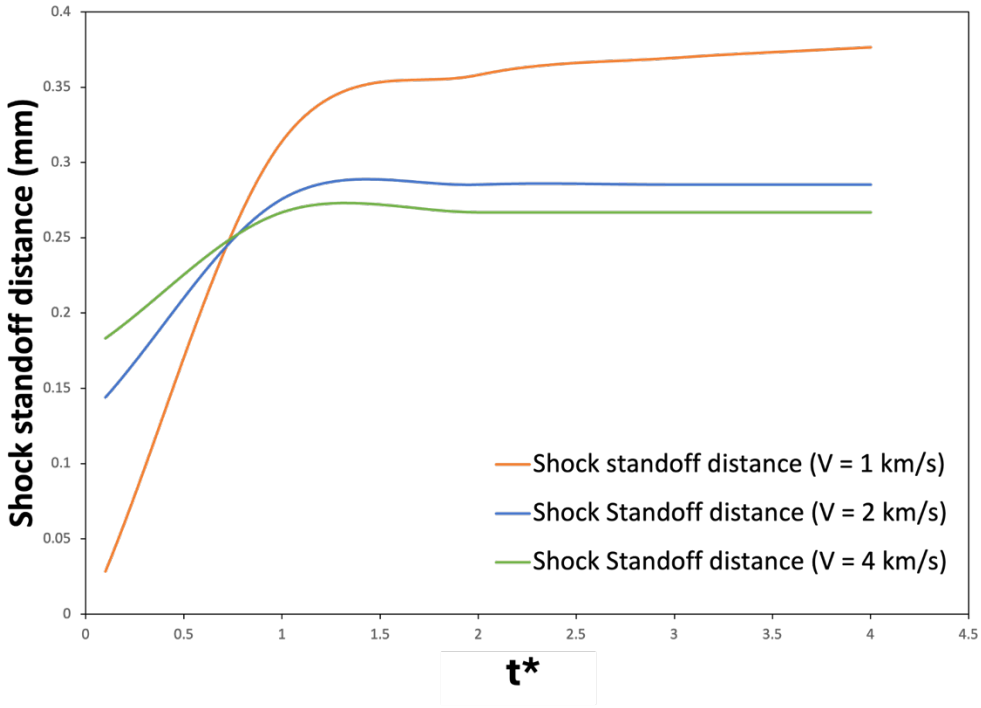

Fig 1.3. Shock standoff distance between the flyer surface and flyer-driven shock wave at velocity of 1, 2 and 4 km/s. Here t* is time and is a non-dimensional number

Similar numerical procedures were followed to model the flyer at a velocity of 1 and 4 km/s. Fig 1.3 presents the shock standoff distance for all the three velocities (1, 2 and 4 km/s) evolving with time, in which the shock standoff distance for velocities 2 and 4 km/s become independent of the flyer velocity which corresponds to Oswatitsch's Mach independence principle, i.e., at extremely high flight Mach number, certain aerodynamic properties become constant.

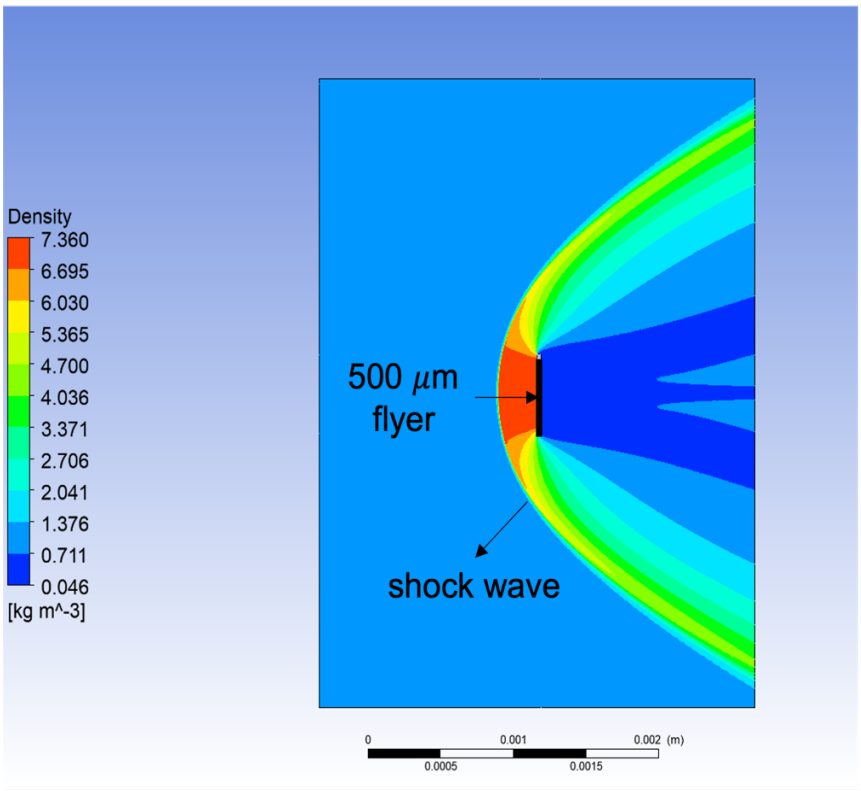

Fig 1.4. Density contour of flyer modeled at a velocity of 2 km/s

In addition, to the numerical analysis of flyer-driven shock wave propagation, the flow immediately behind the flyer was also modeled using a 2D ANSYS-FLUENT solver at a velocity of 2 km/s under STP conditions in air. Fig 1.4 presents the density contour of the flow surrounding the flyer in a steady state from which it can be observed that the density in front of the flyer surface of magnitude 7.360 kg/m^3 (red contour in Fig 1.4) is 20 times higher than the density behind the flyer of magnitude 0.38 kg/m^3 (dark blue contour in Fig 1.4). Here, the density of 0.38 kg/m^3 is an average of 0.046 and 0.711 kg/m^3 shown in the color bar of Fig 1.4. Consequently, the significant difference in density across the flyer leads to material deformation which cannot be observed in Fig 1.4 due to solver limitations. However, in the actual experiment, the flyer deforms from flat to curve shape due to significant flow discrepancies.

1.3 THESIS OBJECTIVES

In this work, the instrumentation of laser-driven flyer is used to design experiments to study topics of interest in hypersonic research. The specific objectives in this endeavor are listed below:

1. Use of available instrumentation in Dr. Dlott's lab to perform high-speed impact test.
2. Identify the limitations of the available instrumentation and diagnostics and develop a new laser-launched flyer apparatus capable of launching larger, denser metal foils to higher velocities with orthogonal line-of-sight imaging ports to follow the hypersonic flyer launch event.
3. Using the shadowgraph and schlieren imaging techniques, capture the flyer-driven shock formation and characterize shock features such as stand-off distance and shock wave shape feature.

CHAPTER 2: USING LASER-DRIVEN FLYERS TO STUDY HYPERSONIC IMPACTS

2.1 INTRODUCTION

To generate shock waves in gaseous and condensed media or to simulate projectile impact with hypersonic vehicles, laser-driven flyer plates provide an invaluable opportunity for prototyping and preliminary science-driven exploratory work. This chapter focuses a specific use-case to showcase the implementation of an existing high-throughput benchtop laser-driven flyer plate setup (extensively used in the past to shock-compress explosives [2][3][4]) by conducting high-speed projectile impacts of micron-sized aluminum flyers on aluminum targets at a velocity ranging 2 to 4 km/s. Given the comprehensive application of aluminum in producing engine and airframe components of high-speed vehicles, in this study, aluminum of different thickness (12.5, 25, 50, and 75 μm) are used specifically as targets to study material response including impact induced cratering and deformation behavior of the aluminum target when subjected to impacts with a variety of energies.

2.2 EXPERIMENTAL DESIGN OF FLYER-BASED IMPACT TESTING

The shock microscope setup employed in this work is used extensively for the study of energetics and condensed matter as detailed in [2][3][4]. In-depth information and specifics regarding the setup can be found in reference [1]. The fundamental basis for flyer generation is a spatially homogenized laser pulse that is focused onto a metal foil mounted onto a glass substrate using epoxy to punch out a metal disk, accelerated by the laser-ablated epoxy glue to impact target placed deliberately in its path. Based on the focusing lens employed the thickness, diameter and the material composites of the flyer can be varied[1]. Additionally, the flyer velocity can be selected

by tuning the laser power. Together these instrumental and experimental parameters offer flexibility in dynamically transferring kinetic energy to any desired test-target.

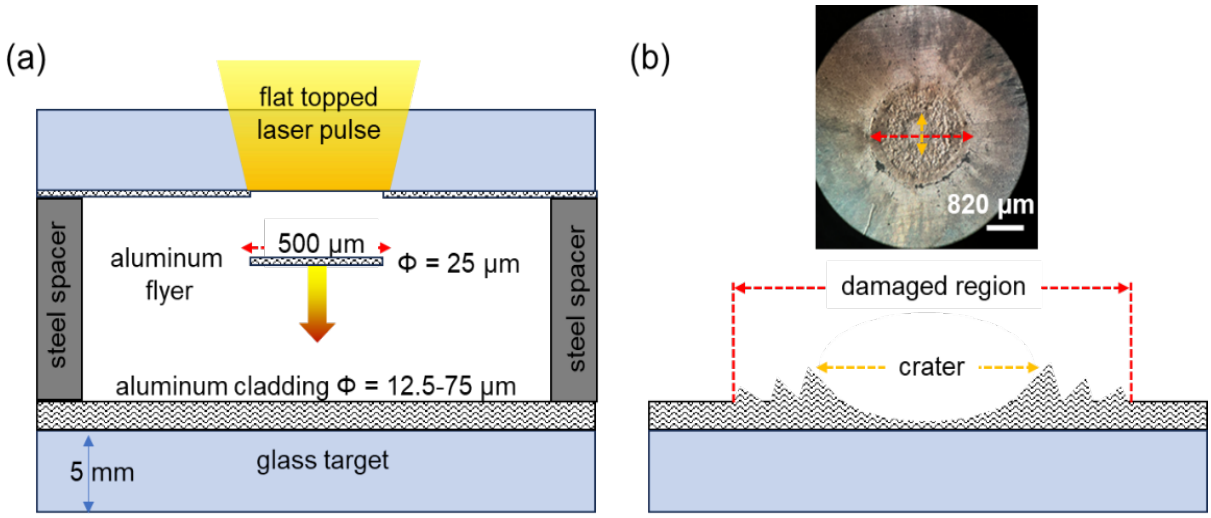

Fig. 2.1 Simplified schematic showcasing (a) the elements within the sample holder along with (b) the features of an impacted target. The inset provides the top view of the actual impact crater and surrounding damage region of 75 µm thick aluminum clad glass substrate impacted by a flyer ay 4 km/s as an example.

Fig 2.1a presents a simplified schematic of the cross-section of the sample holder focusing on the elements of relevance. As shown in Fig 2.1a, in this work, the instrumentation was set up to punch out 0.5 mm diameter flyers out of 25 µm thick Al-1101 foils epoxied on 3x3 inch glass. The flyer velocity was varied between 2-5 km/s (µm/ns) by attenuating the laser power. The flyer substrate is separated from the target by a steel spacer of 380 µm thickness to allow for the flyer to accelerate and attain its terminal velocity prior to impact. The flyer velocity was measured using PDV (Photon Doppler Velocimetry) discussed in detail in [1]. The sample holder is sealed and allows for the control of chamber atmosphere and vacuum pressure. This exploratory work was performed exclusively in STP conditions in an atmosphere of air.

The proposed experimental approach is showcased using quartz glass as the stand-in for test material of interest with a range of aluminum foils of different thicknesses 12.5, 25, 50 and 75 μm as cladding material to protect the glass underneath. These targets were prepared by epoxying aluminum foil onto 5 mm thick 3x3 inch quartz glass (the same as flyer substrates) and annealed at 80° C for 2 hours. The targets were then loaded into the sample holder as seen in Fig 2.1a and impacted by 25 μm thick Al at a variety of flyer velocities 2 - 4 km/s. At least ten repeat runs were conducted at every flyer velocity. The impacted targets were then collected for postmortem analysis to optically image the damaged regions. Fig 2.1b shows the schematic diagram of the central crater and the surrounding damaged region along with the inset showing the top view of one such crater observed after experimentation. The damage can be quantified in several ways, in this work, we focus on the diameter of the craters and the total damaged regions.

2.3 RESULTS & DISCUSSION

The representative images of impact craters caused by a range of flyers on targets clad with different aluminum thicknesses are collected in Fig 2.2. The imaging magnification of the craters were fixed with the use of 5X objective, hence the white scale bar of 820 μm presented in Fig 2.2 is the same for all the images. Fig 2.2 shows a significant increase in damaged area with flyer velocity for all thicknesses of aluminum cladding while the change in impact crater with cladding material thickness is not qualitatively apparent. Using circular fits to bound the central crater and the overall damage area we infer the crater diameter and the damaged region diameter.

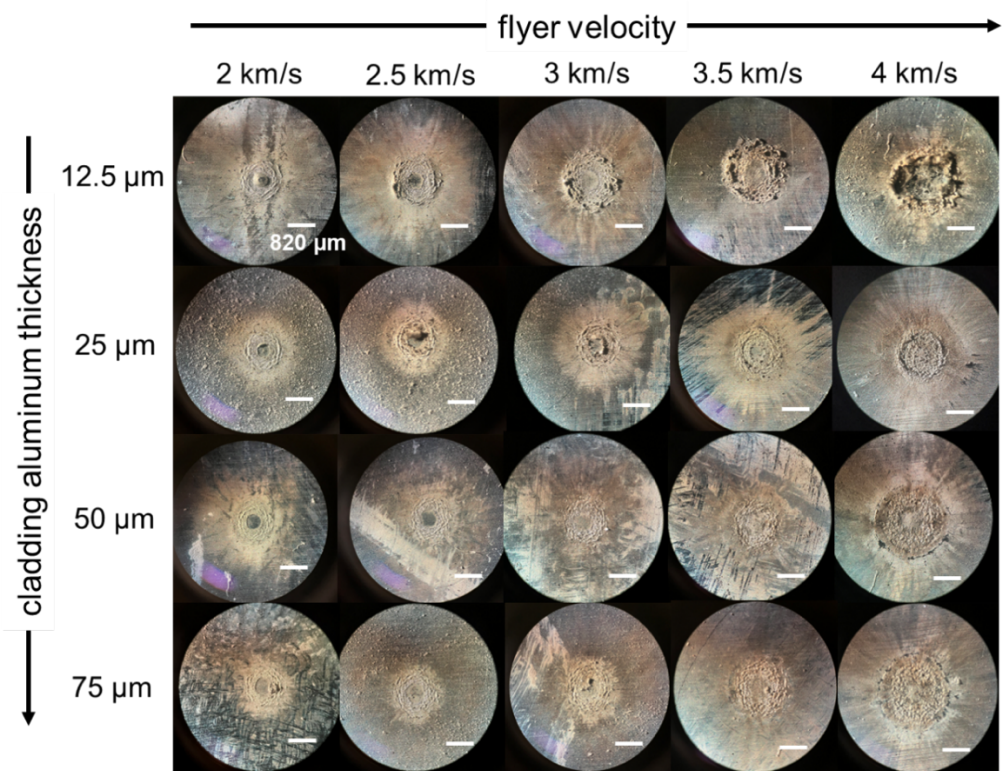

Fig. 2.2 Representative impact craters and surrounding damage observed when 12.5-75 µm thick aluminum clad glass substrates were impacted by 25 µm thick and 500 µm diameter circular aluminum flyers at 2-4 km/s terminal velocities. The white scale bar for the individual images is 820 µm.

Fig 2.3 presents the measured diameter of damaged region and the diameter of the central crater of the tested aluminum clad glass targets along with an unprotected glass target for comparison. The measured diameters are presented as a function of kinetic energy of the flyer, calculated by estimating mass of flyer (1.32×10^{-8} kg) using its dimensions and its measured velocity. As expected, Fig 2.3 shows the effectiveness of aluminum cladding in protecting glass targets resulting in smaller craters (unfilled circles) while the naked glass target suffered more damage with bigger diameter craters (unfilled stars) across the range of impactor velocities explored. The energy absorbed by the cladding material is clearly dispersed within the aluminum layer seen by the large extended damaged region (solid filled circles). However, in the range of aluminum foil

thickness tested no significant difference in behavior is observed. All the cladded targets exhibited very similar behavior despite the difference in thickness.

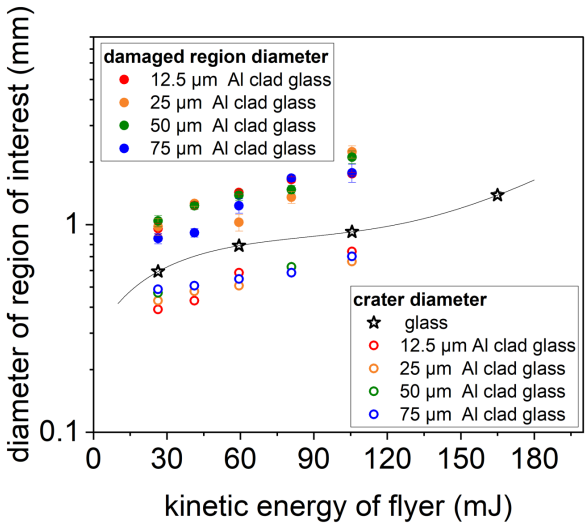

Fig. 2.3 The diameter of damaged region and the diameter of the central crater of the impacted 12.5-75 µm thick aluminum clad glass substrate presented as a function of flyer kinetic energy. The crater diameters of similarly impacted unclad-glass substrate is also provided as a baseline. The solid line, a cubic fit of the unclad glass data is added as a visual aid.

The crater diameters of all the aluminum clad glass targets for a given flyer velocity are averaged and presented as a function of their kinetic energy to enable comparison with other large-scale gas-gun experiments collated in Fig 2.4. These specific data sets were chosen as they employed aluminum projectiles to impact aluminum targets, similar to current work. But these gas-gun experiments used spherical pellets of significantly higher masses ranging from 0.2 g to 1.7 g as compared to 1.32 x 10^{-5} g flat circular foils used in this work. Additionally, the target architecture was significantly different using 18 cm thick aluminum monolithic block [5] or three aluminum bumpers of 1.2, 0.8 and 2.8 mm thicknesses separated by 60 mm acting as a composite shield [6]. Despite the differences, the crater diameters obtained in this work when extrapolated to the high

energy projectile space provide very reasonable damage estimates in the ballpark of previously observed impact craters in gas-gun experiments.

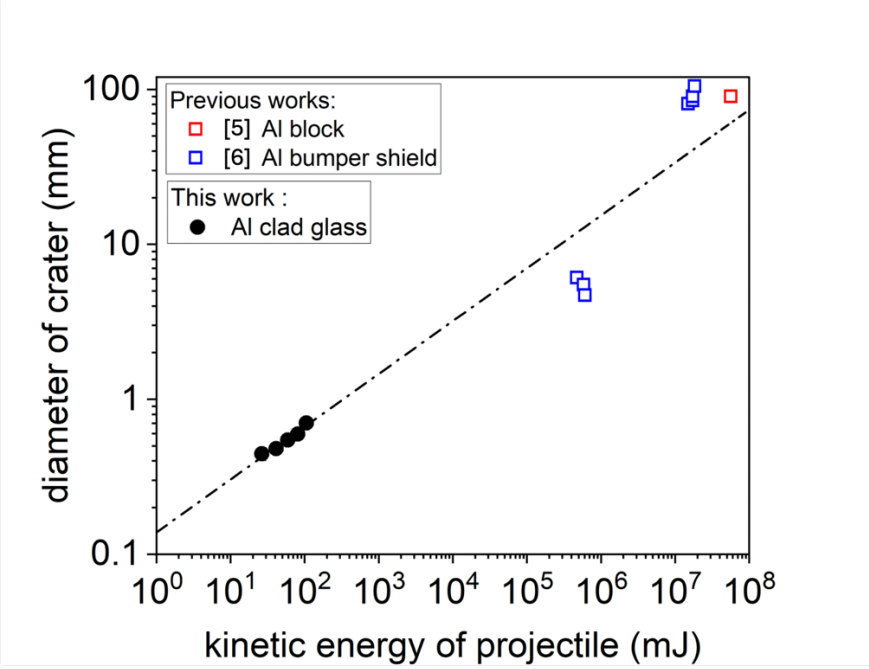

Fig. 2.4 The diameter of the impact crater as a function of the kinetic energy of the projectile obtained in this work along with previously reported works [5][6]

2.4 CONCLUSION

The proposed application of laser-driven flyer plates as a high-throughput characterization tool to hasten development of prototype shield/cladding material for high-speed vehicles and spacecrafts shows promise. In this study, aluminum clad glass targets were impacted by hypersonic projectiles as proof of concept and the impacted targets were analyzed postmortem. The small-scale benchtop experimentation in this work was shown to be scalable to draw inferences applicable to large scale experimentation involving gas-guns. Acknowledging the impracticality of the aluminum clad glass targets tested in this work, a more detailed experimentation using near-practical targets of appropriate materials and accounting for shield architecture is necessary. Additional in-situ characterization in the form of high-speed imaging to capture impact events and subsequent debris

breakup as well as hyperspectral imaging to map impact emissions and derive temperature estimates would be invaluable for modeling and understanding the impact phenomena. In-depth ex-situ post-mortem characterization of the impacted targets to access damage such as crater depth is pertinent to help compare with more large-scale experimental data currently available.

2.5 LIMITATIONS OF CURRENT SETUP AND OPPORTUNITIES

The use of a table-top high throughput setup to study supersonic and hypersonic phenomena is immensely useful for aerospace and aeronautic engineering. Preliminary experimentation on the presented laser-launched flyer setup can be used to study various topics of interests beyond high-speed impact dynamics, such as material spallation, debris formation after impact, shock formation and its stability in hypersonic flight, shock/flow field and debris interaction, among many others.

However, the existing Nd: YAG laser-driven flyer experimental setup in Dr. Dlott's lab has design constraints as its intended application was to study shock-initiated reactions in energetics which limit the setup in exploring a wide gamut of scientific questions in hypersonics. In this benchtop setup, the test section is built to launch the flyers only in the vertical direction in reference to the optical bench and there is no dedicated optical window to image the profile view of the flyer and target. Further the Nd: YAG laser used in the setup cannot generate sufficient energy to drive thicker or bigger flyers and flyers made from denser metals to higher terminal velocities to deliver a variety of shocks to solids and gaseous media.

To overcome these constraints, a new setup with a more powerful Nd: Glass laser is built, through which it is possible to launch the flyer in both vertical and horizontal direction in reference to the optical bench. This will allow us to study the impact test in both orthogonal and parallel plane in reference to the flyer launch direction. Further, the Nd: Glass laser can offer up to energy

of 8 J unlike Nd: YAG laser which has a maximum laser power output of 2 J. Given the high laser energy from the Nd: Glass laser, it is possible to launch flyers of various composites in supersonic/hypersonic speed allowing the possibility to perform other application-based studies apart from impact test including the simulation of hypersonic flow, and study various aspects of shock-wave droplet interaction to probe physics of rotating detonation engines. The following sections provide a brief description of the components involved in the Nd: Glass laser-driven flyer benchtop instrumentation and the imaging diagnostics required to model the hypersonic flow field, the central focus of this thesis.

2.6 REFERENCES

[1] Shaw. W. L, "Reactive solids under shock compression," PhD dissertation, Department of Chemistry, University of Illinois Urbana-Champaign, Illinois, 2016

[2] Brown. K. E., Shaw. W. L., Zheng. X., and Dlott. D., "Simplified laser-driven flyer plates for shock compression science," *Review of Scientific Experiments*, Vol. 83, No. 10, 2012
Doi: 10.1063/1.4754717

[3] Bhowmick. M, Bassett. W. P., Matveev. S., Salvati III. L., and D. D. Dlott, Optical windows as materials for high-speed shock wave detectors, *AIP Adv.* 8, Vol. 8, 2018
Doi: 10.1063/1.5055676

[4] Banishev. A. A, Shaw W. L., Bassett W. P., and Dlott. D., High-speed laser-launched flyer impacts studied with ultrafast photography and velocimetry, *J. Dyn. Behav. Mater.* 2, Vol. 2, 2016
Doi: 10.1007/s40870-016-0058-2

[5] Syed. A. K., Fitzpatrick. M. E., Moffatt. J. E., Doucet. J., and Durazo-Cardenas. I., "Effect of impact damage on fatigue performance of structures reinforced with GLARE bonded crack retarders," *International Journal of Fatigue*, Vol. 80, 2015
Doi: 10.1016/j.ijfatigue.2015.06.006

[6] Lambert. M. and Schneider. E., "Shielding against space debris. A comparison between different shields: The effect of materials on their performances," *International Journal of Impact Engineering*, Vol. 17, 1995
Doi: 10.1016/0734-743X(95)99872-O

CHAPTER 3: DEVELOPMENT OF HIGH-ENERGY LASER-LAUNCHED FLYER INSTRUMENTATION AND ASSOCIATED HIGH-SPEED IMAGING DIAGNOSTICS

3.1 INTRODUCTION

The instrumentation for laser-driven flyer plates is well established and in use currently in several research labs including Dr. Dlott's lab at UIUC [1,2,3,4]. The central idea in generating flyers is to focus a flat-topped IR laser pulse onto a metal foil glued to glass. The glue vaporizes after absorbing a portion of the energy from the pulse, punching out a nearly circular foil and driving it to supersonic/hypersonic speeds. Using the same principles established in [5], we built a new setup driven by a laser with higher energetic output to launch thicker or wider flyers, or flyers of a wider variety of denser metal foils or to simply launch conventional aluminum flyers to higher terminal velocities.

The Fig 3.1 presents the optical elements used to set up a more powerful and versatile instrumentation along with a schematic representation. The pulse exiting the IR laser (labelled 1 in Fig 1a and b) is first attuned by the variable attenuator (labelled 2) to a desired energy and shaped by the beam shaping optics (labelled 4) to launch flyers out of metal foils. As the laser pulse is trained onto a reflective element, a Faraday isolator (labelled 3) is used to prevent any back-reflected light from entering the laser. Finally, a back-lit optical setup observed by a high-speed camera (labelled 5) is employed to capture the flyer travelling across the field of view along with the fluid flow fields around it. Additional in-line view of the flyer is possible in future, similar to the previously described Nd:YAG launched flyer system in Chapter 2. In the current work, since the focus is to capture shock formation ahead of the hypersonic flyer plate the imaging diagnostics are setup as shown in Fig 1 to capture the profile of a launched flyer plate.

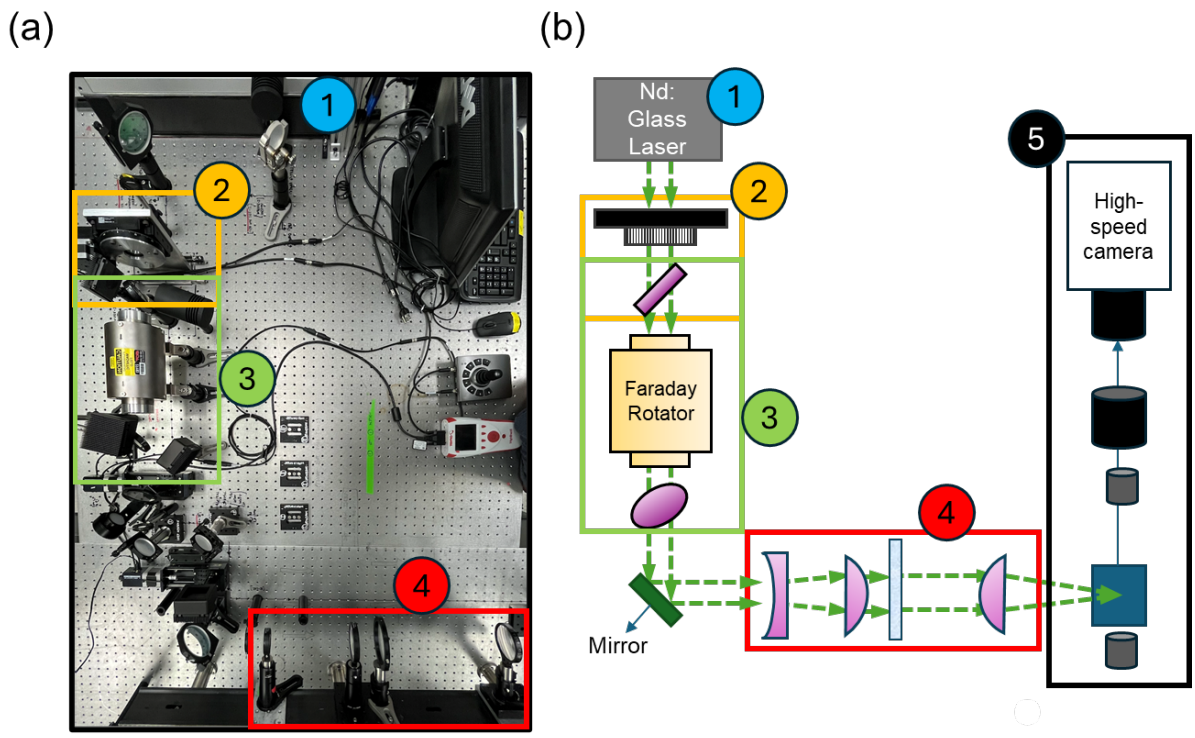

Fig 3.1. (a) The top-view of the actual image of the instrumental setup on the optical bench along with its (b) simplified schematic representation. The labelled, color-coded components in both are: 1- Nd: Glass Laser, 2- variable attenuator (for tuning laser pulse energy), 3- Faraday isolator (as a safety mechanism to stop redirected light entering the laser), 4- beam shaper (to achieve a flat-topped beam to punch flyers) 5- imaging diagnostics (to observe the flight of the flyer and bow shock ahead of it).

The subsequent sections delve deeper into the specific details and function of each of the elements introduced in Fig 3.1 to provide a wholistic understanding.

3.2 HIGH-ENERGY LASER

The Nd: Glass laser employed in the new setup - a custom-built multimode laser by Continuum® - operates at a wavelength of 1053 nm due to its use of phosphate optical glass to achieve lasing action and is capable of delivering a maximum energy of 8 J per pulse every 10 seconds with a pulse duration of 35 ns. The schematic diagram of the internal elements of the specific version of laser used in this setup are shown in Fig 3.2.

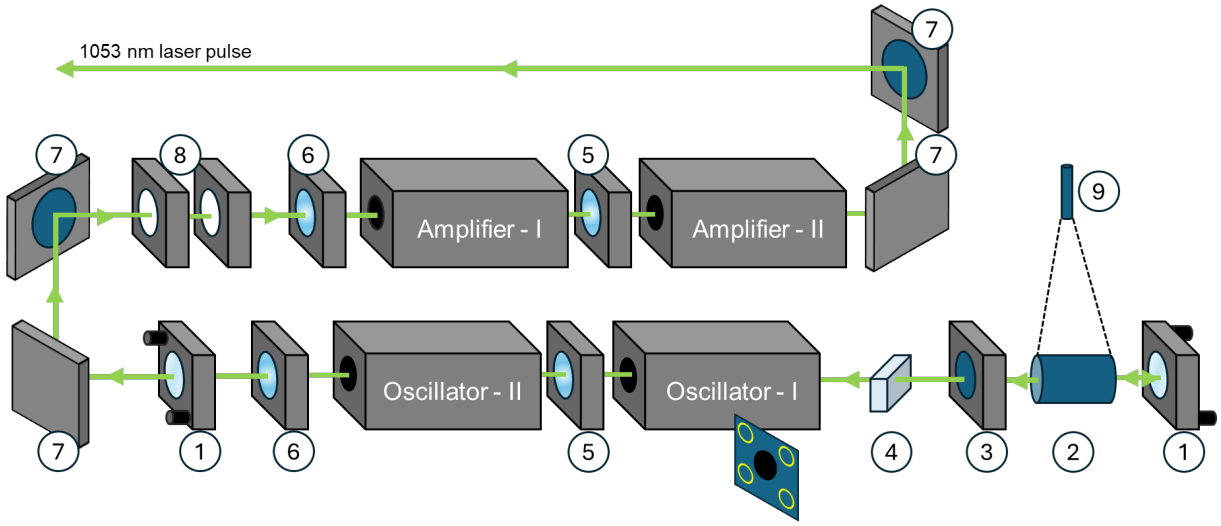

Fig 3.2. The schematic diagram on the internal components of the custom-built Nd: Glass laser manufactured by Continuum®. The numbered components in the schematic are: 1- end mirror, 2- Pockel cell (Q-switching element), 3- quarter waveplate, 4- polarizing beamsplitter (set to reject vertically polarized light), 5- zeroth order bifringence nullifier (necessary since our gain medium is phosphate glass), 6- apodizer (optic to adjust beam profile into a circle), 7- corner mirror, 8- telescopic lens setup (to increase beam diameter) and 9- photodiode trained at the Pockel cell to follow emissions accompanying Q-switching. A section of the four flashing lamps housed within the oscillator/amplifier heads is shown beside oscillator-I. The green line pictographically tracks the path of light through all the components.

The gain medium, the Nd: glass rods within the oscillator/amplifier heads are optically pumped using four flash lamps per head. The four flash lamps are arranged as vertices of a square drawn around the central axis (green line) (see description of Fig 3.2) and in successive oscillator/amplifier heads this lamp arrangement is rotated by 22.5 degrees to effectively fill the circular space about the central axis. As shown in Fig 3.2, the Pockel cell in tandem with the initial polarizer and waveplate (elements 1-3 in Fig 3.2) functions as a 'shutter' capable of opening very quickly in < 2ns and closing much slower ~1ms such that when the gain medium has desired population inversion, we create a short duration high-energy laser pulse. The Pockels cell has sufficient time to return to its initial state by the time for the next pulse 10 seconds afterwards. The optical pumping by the flash lamps occurs over several hundreds of microseconds and the timing

of Q-switching is important to extract maximum energy. During operation the oscillator and amplifier heads are actively cooled by flowing distilled water through the optical cavities of these units which is subsequently cooled by an external secondary water line.

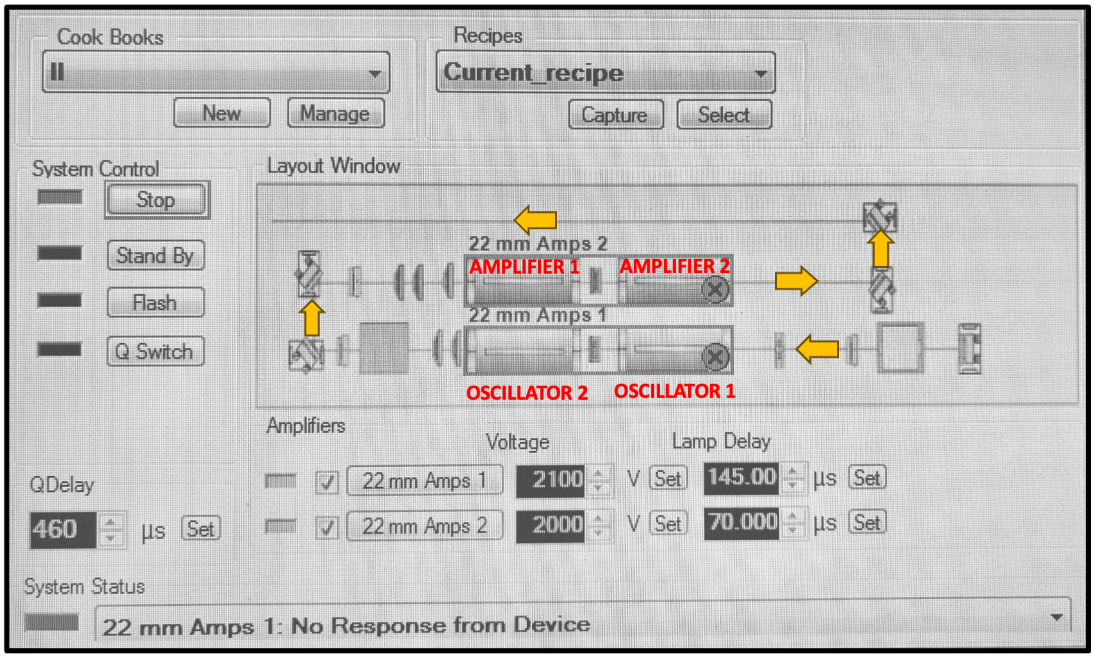

Fig 3.3. A snapshot of the primary GUI of Amplitude continuum software highlighting the control elements to tune the Nd: Glass laser used in this instrumental setup.

The entire laser unit is controlled by the Amplitude software from Continuum®. Fig 3.3 shows the GUI of the Amplitude software. The layout window in the Fig 3.3 provides the top-view of the two oscillators and amplifiers heads positioned similar to the schematic in Fig 3.2. The flashlamps within each of these amplifier and oscillator heads are triggered using a pulse generator that the GUI controls. Under the system control, the stop button is used to turn on or tun off the laser, the standby button is used to initiate the water flow and low voltage housekeeping checks in the system, while the flash button is used to enable the flash lamp system and the Q-switch button enables emission (Note: It is important to allow the system to 'flash' for 30 minutes without Q-

switching. This will allow equilibration of the poorly conductive gain medium, i.e., the phosphate glass).

When the Flash button is turned on, the flashlamps inside the oscillators will get triggered first followed by the amplifiers. The lamp firing inside these oscillator and amplifier have a delay of 70 and 145 μs, respectively (as shown in Fig 3.2), such that the laser power output is maximum. In case the timing of the optical pumping of the oscillators and the amplifiers are skewed significantly, the amplifiers will not amplify the laser input received from the oscillator and reducing the overall output to that of the oscillator alone ~2.5 J.

In addition to the lamp delay, another important electronic delay to note is the QDelay. The QDelay time in the GUI (Refer to Fig 3.3) is set to 460 μs such that the laser produces a Q-switched pulse at the peak of the gain in the laser rods.

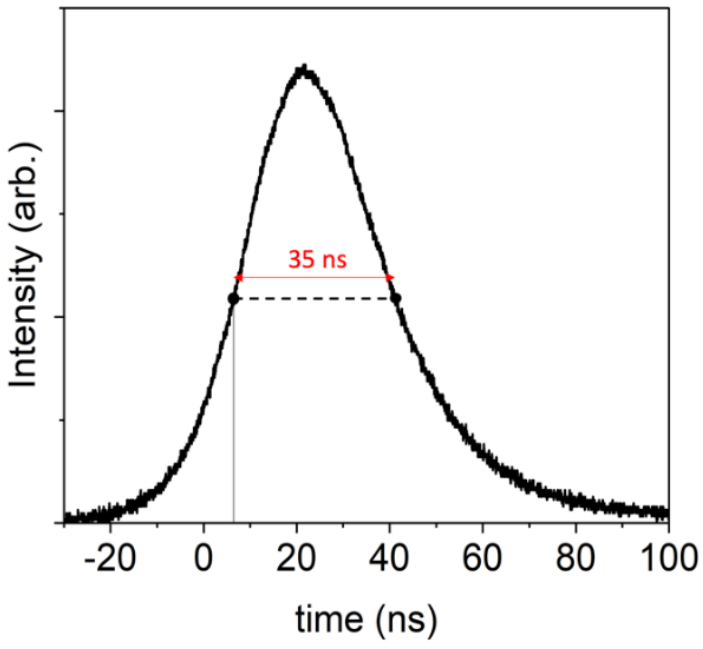

Fig 3.4. Pulse width of the final pulse exiting the Nd: Glass laser calculated as the full-width half maximum, acquired using a photodiode trained at the Q-switching element, the Pockel cell. See Fig 3.2 for the photodiode placement within the internals of the laser.

The pulse duration of this Nd: Glass laser is 35 ns, as evidenced in Fig 3.4, which is three times longer than that of the Nd: YAG laser (whose pulse duration is 10 ns) [1]. Increase in the pulse-width will allow the laser to launch thicker flyers, subsequently, increasing the possibility to test different energy transfer mechanisms.

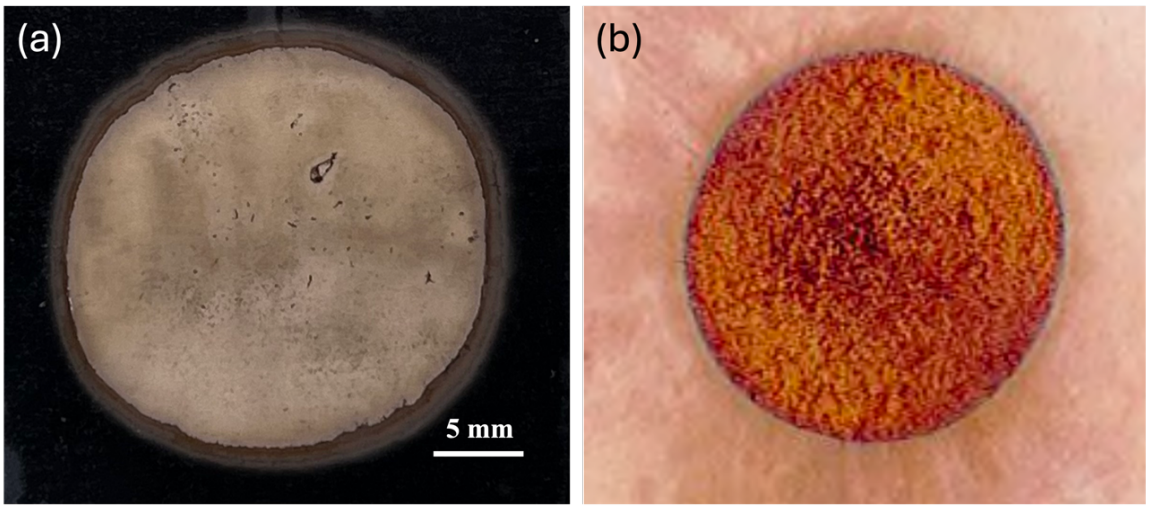

Fig 3.5. Burn spots of custom-built Nd: Glass laser (a) captured in the Dlott's lab and (b) documented in the laser manual showcasing the general shape and spatial spread of laser energy. Any change to the oscillator and amplifier voltages (adjusted using the GUI seen in Fig 3.3) and small adjustment to the end-mirrors bookending both the oscillators and the Pockel cell (seen in Fig 3.2), can modify the shape and energetic output of the pulse.

The general beam shape and size within the laser box is documented using laser alignment/burn papers (acquired from ZAP-IT Laser Alignment Papers). In Fig 3.5a, the burn spot of the laser beam of energy ~ 8 J captured in the Dlott's lab is shown and in Fig 3.5b, the burn spot from the manufacturer manual (Continuum® Amplitude Co-op) is shown for reference. To maintain the beam shape (shown in Fig 3.5), as mentioned earlier, it is important to set the oscillator and amplifier flash lamp voltages to the maximum in the GUI. In addition to that, making sure that the pressure of the external secondary water fed into the primary unit (PU 610K) is in the range of 40 – 60 bar. This is important to consider as the laser rods (cylindrically shaped) are cooled by primary

coolant - distilled water, which if insufficiently cooled by the external water supply, can result in inhomogeneous temperature fields in the laser rods which negatively influences the beam shape.

A rudimentary coarse attenuation of laser power is possible by tuning the amplifier and oscillator voltages between 1700V and 2100V (see GUI in Fig 3.3 to tune voltage) for safe handling during set up of optics and their alignment. But this cannot be used to attenuate laser power to modulate flyer velocities downstream as change in lamp voltages effects the spatial distribution of energy as some modes may vanish below certain optical pumping thresholds. Furthermore, the general spatial inhomogeneity of even a 'good' pulse (observable as variance in damage within burn spot seen in Fig 3.5) makes the flyer launch impossible without the beam shaping component shown in Fig 3.1 (labelled 4).

3.3 VARIABLE ATTENUATOR

The Nd: Glass laser operates on the principle of generating high-energy pulses, capable of delivering up to 8 J of energy. As discussed in the previous section, the energy output can be altered by varying the voltage of the amplifier and the oscillator units. However, the voltage modifies the intensity of the flash lamps in these units and in turn varies the optical pumping of the phosphate rods. Further, the minimum voltage for lasing is limited to 1700 V while the maximum is 2100V for safe operation of the flash lamps. In this range, a non-linear, coarse attenuation of laser power is possible. In addition, since the glass laser is a multimodal laser, the change in voltage also causes complex changes to the spatial distribution and temporal output of the laser energy. This is because at certain voltages, preferred modes dominate while others may cease to contribute, resulting in an inhomogeneous energy distribution.

To overcome these challenges, alternative approach to modulate the laser energy is the implementation of a variable attenuator through which the energy output of the laser can be varied with high tolerance and nearly zero impact on the spatial profile of the beam. In Fig 3.6a and 3.6b, the three important components of the variable attenuator, namely, λ/2 waveplate, polarizing beamsplitter and the beam dump are highlighted on both the actual and schematic diagram, respectively. The λ/2 waveplate (denoted by the red numeral '1' in both Fig 3.6a and 3.6b) consisting of a single crystal quartz cut at a specific angle is installed in a 2-inch aperture of a rotary stage driven by a stepper motor (X-RSB model acquired from Zaber Technologies). Based on the angle of rotation of the stage, the orientation of the quartz crystal is changed to vary the polarization of light passing through it. The 1054 nm polarizing beamsplitter (acquired from Lattice Electro Optics LEO denoted by the red numeral '2' in Fig 3.6a and 3.6b) downstream from the waveplate acts as a barrier, transmitting only the horizontal (w.r.t to the optical table) projection of the light polarized by the waveplate. The vertical component of the light is rejected by the polarizing beamsplitter into the Laser Beam Dump (TRAP-IT™ beam dump supplied by Kentek). As seen in Fig 3.6a, the polarizing beamsplitter is installed at an angle of 57° to the incident beam so that most of the horizontally polarized incident light (98%) is transmitted and nearly all (99%) of vertically polarized light is reflected.

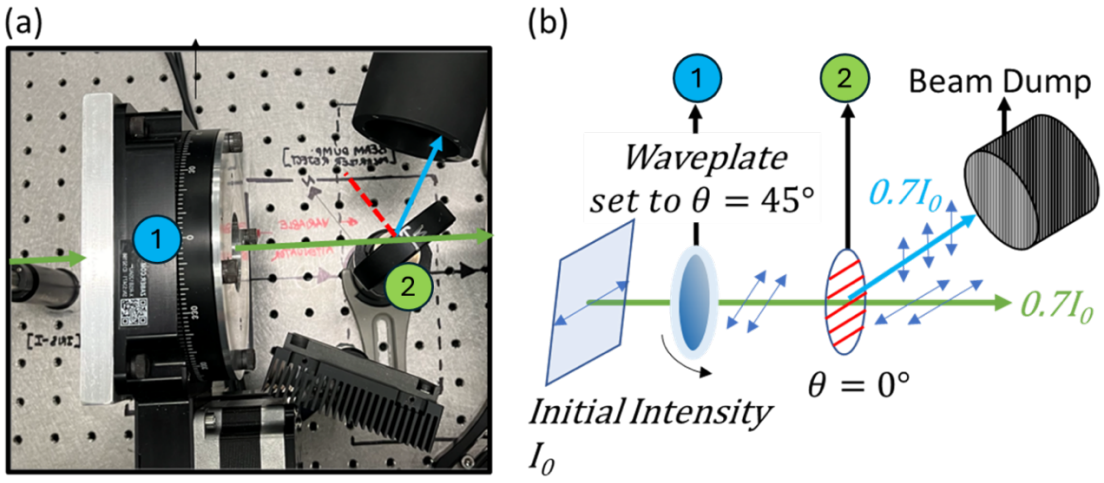

Fig 3.6. (a) Actual image of variable attenuator setup along with (b) a simplified schematic representation showing the polarity and intensity of the light at each step. The color coded and numbered components in both correspond to: 1- λ/2 waveplate and 2-1054 nm polarizing beamsplitter. The green line shows the path of the laser beam while the blue line shows the beam rejected by the polarizer which is directed into the beam dump. In the example depicted, the λ/2 waveplate rotates the beam polarization by 45 °.

Fig 3.6b showcases an example to further elucidate the attenuation process. As shown in the schematic, the horizontally polarized light of intensity I_0, leaving the laser box is rotated 45° by the variable waveplate before it encounters the polarizer. The polarizer then transmits the horizontal component such that ~0.7 times the initial intensity is allowed downstream. In this fashion the laser beam can be finely attuned by rotating the λ/2 waveplate without any undesired changes to the spatial or temporal robustness of the beam.

Fig 3.7 showcases attenuation range by plotting the intensity of light leaving the variable attenuator as a function of the angle of rotation of the λ/2 waveplate when both oscillator and amplifier are operated, and only when the oscillator is operated. A beam splitter is placed in the path of the light exiting the attenuator such that it reflects 6 % of incident light into a power meter (StarBright Laser Power & Energy Meter from Ophir). The orientation of the power meter is at an angle of 45° to the laser path. The highest observed energy when both oscillator and amplifier are operated is 7.3

J (91% of the 8 J of the out-of-the-box pulse energy), 4.9 x higher energy than previously used Nd:YAG laser [1] while the minimum registered value was 450 mJ.

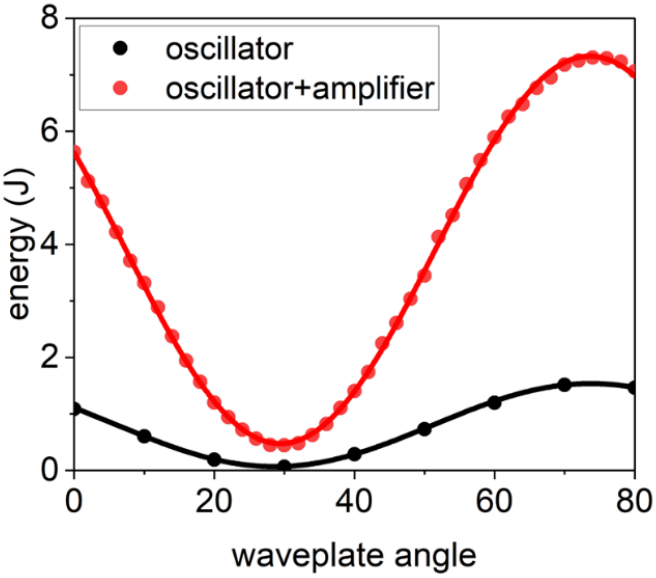

Fig 3.7. Laser energy measured after the variable attenuator presented as function of waveplate angles when only oscillator is operated and when both oscillator and amplifier are operated. The smooth lines are trigonometric sine function fits of the experimentally obtained values. Each point is the average of 10 energy measurements made at a specific λ/2 waveplate rotational angle.

3.4 FARADAY ISOLATOR

The laser-launched flyer setup comprises of a highly reflective metal foil at the end of the line, as well as optical components along the way that may have a small degree of reflectance. Ensuring the integrity of the laser demands the prevention of beam redirection into the Nd: Glass laser. The blocking of any reflected light entering the laser is achieved through an optical device called the Faraday isolator. Fig 3.8a and 3.8b presents the actual image and the schematic of the Faraday isolator composed of a Faraday rotator (acquired from EOTech) positioned between two 1054 nm polarizing beamsplitters with different orientation (acquired from Lattice Electro Optics LEO).

In this configuration, polarizing beamsplitter-I introduced earlier in the attenuator section selectively permits horizontally polarized light and polarizing beamsplitter-II allows the transmission of 45° polarized light. The Faraday rotator, a permanent magnetic rotates the polarization of the light passing through its aperture by an angle of 45°.

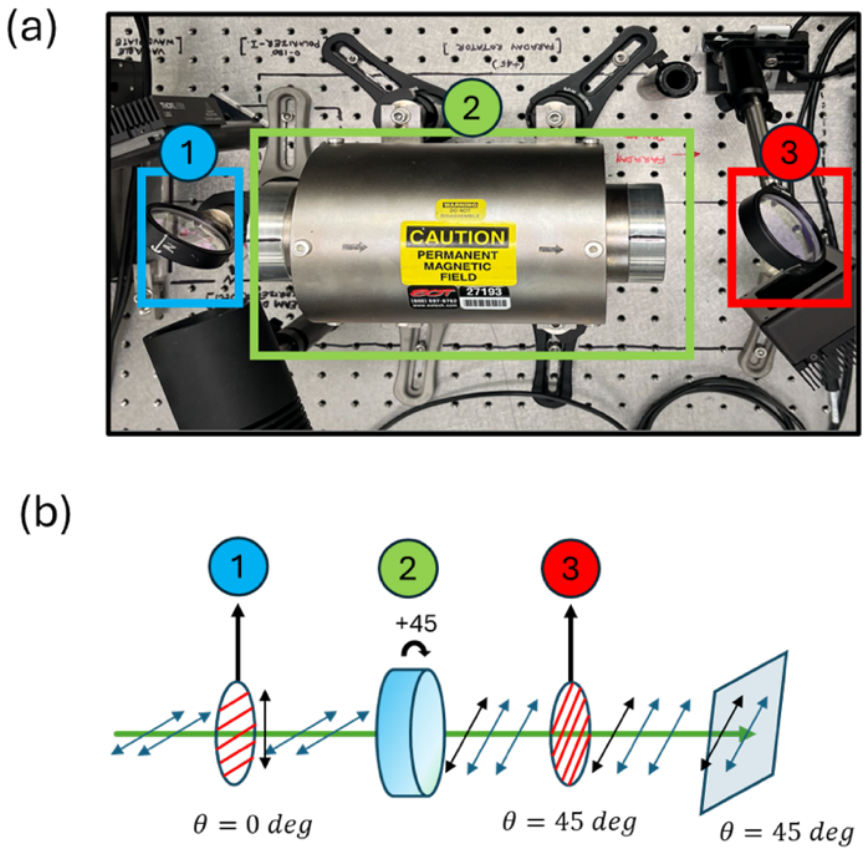

Fig 3.8. (a) Top-view image of the actual experimental setup and (b) schematic diagram of the faraday isolator. The numbered components in both are: 1- polarizing beamsplitter-I, 2-faraday rotator, and 3- polarizing beamsplitter-II.

The strategic placement of polarizing beamsplitter-I at 0° and polarizing beamsplitter-II at 45° holds significance in effectively nullifying any light reflecting towards the Nd: Glass laser. As an example, consider the case shown in Fig 3.8b schematic, the horizontal polarized light (denoted by blue “double arrow” before polarizer-I in Fig 3.8b) traverses through polarizing beamsplitter-I

and the beam polarization angle increase to 45° (denoted by blue “double arrow” behind faraday rotator in Fig 3.8b). The resulting 45° polarized light traverses through polarizing beamsplitter-II (denoted by blue “double arrow” behind polarizer-II in Fig 3.8b). However, when the reflected 45° polarized light (denoted by black “double arrow” before polarizer-II in Fig 3.8b) passes through the faraday rotator, the polarization angle increases to 90° (denoted by black “double arrow” before faraday rotator in Fig 3.8b). This 90° polarized light is completely rejected by polarizing beamsplitter-I as it only allows horizontally polarized light. This design principle underscores the efficacy of the Faraday isolator in safeguarding against unforeseen beam redirection.

In summary, the configuration of polarizing beamsplitter I and II at specific angles, combined with the Faraday rotator, ensures optimal transmission of the beam while safeguarding against undesired reflections. It’s important to note that throughout the variable attenuator and Faraday isolator, the laser beam retains its beam profile, with no alterations in beam size.

3.5 BEAM SHAPER

The beam shaper setup serves a specific function: to modify the laser beam profile into a top-hat profile. As previously discussed, the inherent laser profile from the Nd: Glass laser system is ‘near-gaussian’. However, such an energy distribution results in an undesirable outcome where the laser pulse driven ablation unevenly drives different parts of the flyer to move at different speeds so the flyer tears itself apart instead of launching a mechanically intact flyer [6]. To ensure the production of a flyer, it is essential to evenly spread the energy over a major portion of the focal plane. The Fig 3.9 presents the actual image of the optics used and elucidates their role using a schematic and presents burn spots at various points to showcase the effects of each of the components.

The beam shaper has four optical components strategically positioned to achieve the desired top-hat beam profile. These components consist of a plano-concave lens with a focal length of -125mm, a plano-convex lens with a focal length of +300 mm, a beam homogenizer (sourced from Silios, Inc.), and a focusing lens whose focal length is adjustable within the range of +150 to +300 mm.

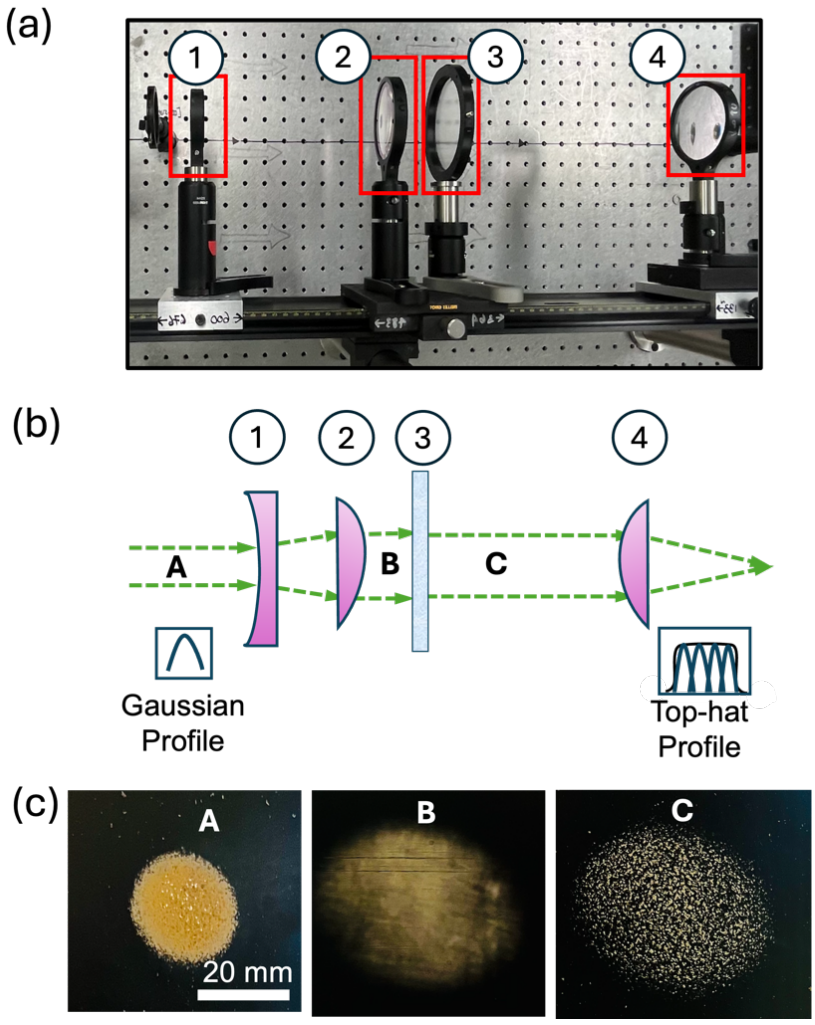

Fig 3.9. (a) Actual image and (b) schematic diagram of the beam shaper composed of the optical elements labelled in both as: 1- plano concave lens, 2- plano convex lens, 3- homogenizer, and 4- focusing lens (to focus the homogenized beam into an appropriate size to launch flyers of desired diameters), along with burn spots acquired at specific locations: A- before the laser hits the plano concave lens, B- after the plano convex lens and C- after the homogenizer. The scale for all three burn spot images is the same.

Among these optics, the plano-concave and plano-convex lenses combined act as a telescopic setup to enlarge the beam diameter from 20 mm diameter to 40 mm as shown in the schematic of Fig 3.9b and evidenced by increase in size of burn spot 'A' into 'B' as shown in Fig 3.9c. The beam after the telescopic setup is collimated for a reasonable distance. This enlarged spatially inhomogeneous beam traverses through a beam homogenizer which is crucial to achieve a flat-top profile. The homogenizer is a diffractive optic with uniformly spaced tiny gratings, that diffract light into a uniform disk. Each of the disk of diffracted light is superimposed with surrounding disks of diffracted light to result in a homogenized distribution of intensity as seen in the burn spot transformation from the inhomogeneous cloud-like burn pattern seen in 'B' to the ordered speckle of nearly identical burn damage across the entire space as seen in 'C' in Fig 3.9c. Refer to the cartoon showcasing this change in a pictographic representation in Fig 3.9c.

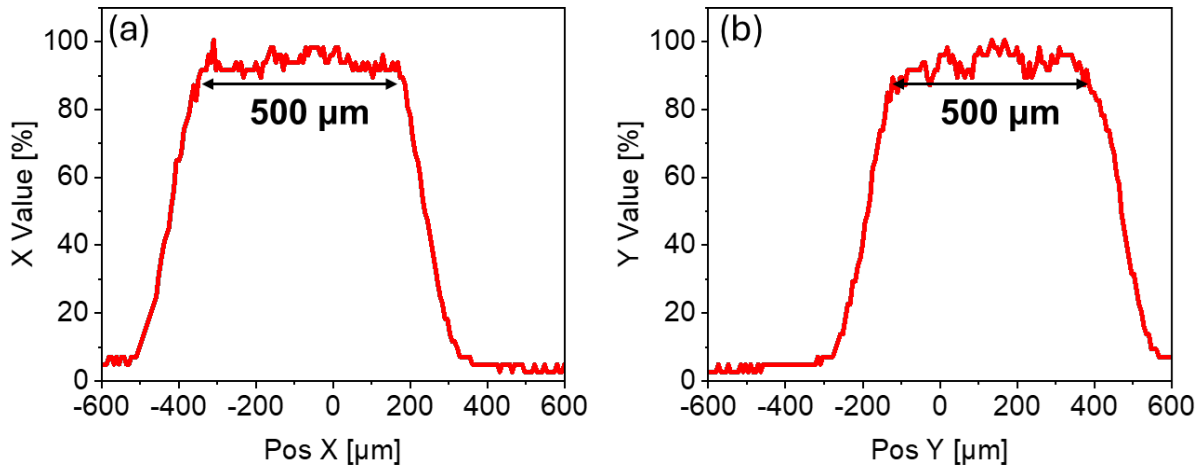

Fig 3.10. The laser pulse intensity across x and y axis of the homogenized beam profile at the focal point. Note the spot is not centered on the beam profiler sensor but shows the flat top of 0.5 mm diameter necessary for launching flyers.

Subsequently, by passing through the focusing lens, these discrete points come closer to form a uniform flat-topped profile of a 0.5 mm diameter circle at the focal point of the lens. In this fashion the homogenizer can treat nearly any incident beam into a top-hat profile in the far field. The diameter of the focal plane of the final focusing lens dictates the diameter of the flyer we can launch. This focal point essentially is expected to translate to the diameter of the metal foil punched out by the shaped pulse. The intensity plots along x and y axis of the flat-topped profile of the beam are presented in Fig 3.10, captured using an 8.8x6.6mm apertured Thor Labs camera beam profiler (BC106N-VIS).

3.6 CAPABILITIES OF NEW LASER-DRIVEN FLYER INSTRUMENTATION

As discussed in the previous sections, the new laser-launched flyer plate apparatus is capable of delivering flat-topped shaped pulses of upto 8 J energy. Prior unpublished work on this instrumentation explored its capability of launching flyers out of different metal foils of multiple thicknesses and measuring their velocities using photon doppler velocimetry (PDV). Fig 3.11a presents the maximum terminal velocity achieved by the flyers tested for the laser energy used to drive it.

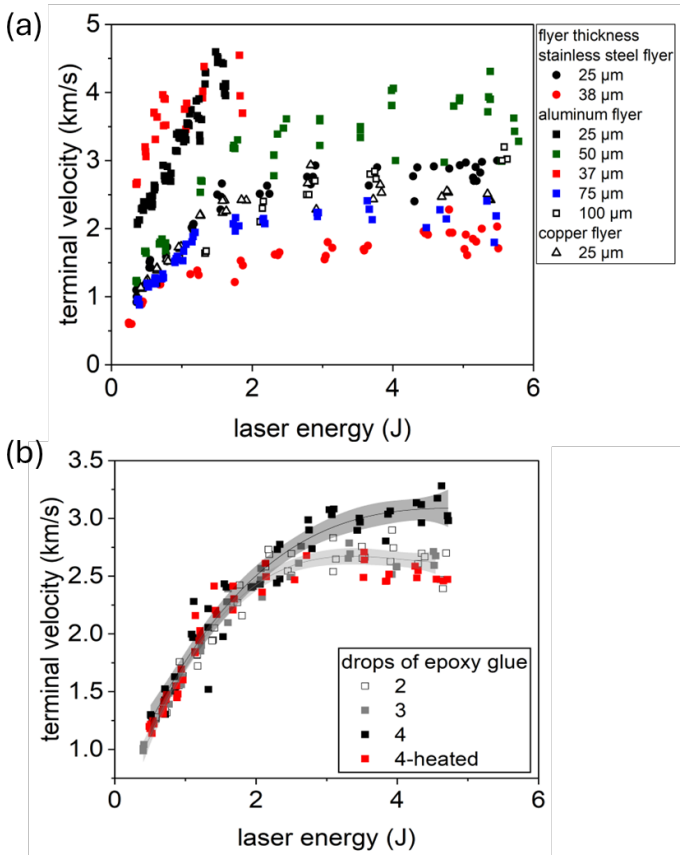

Fig 3.11. The terminal velocities of (a) flyers of different metals and thicknesses launched by the new setup built in this work and (b) terminal velocities of 75 μm thick, 0.5 mm diameter Al flyers prepared with different amount of epoxy adhesive, presented as a function of the laser energy used to launch them.

The Nd: Glass laser is able to pump up to 6 J of energy (after losses due to optics employed) into flyer formation process resulting in the driving of thicker foils such as 100 μm thick aluminum to higher velocities of 2.3 km/s and denser metal foils of the conventional thickness of 25 μm such as stainless steel and copper up to 3 km/s.

To see if the flyer velocities are limited by the amount of ablative sacrificial material available in the focal point, flyers of a given thickness were adhered onto glass substrates with increasing amount of epoxy and tested. Fig 3.11b shows the terminal velocities of 75 µm thick Al flyers prepared using 2-4 drops of epoxy as a function of pulse energy. As is evident from the plot, up to 0.5 km/s increase can be seen with increase in ablative material. So, the terminal velocities of

denser and thicker metal foils presented in Fig 3.11a can be increased, if need be, by adding more ablative material or swapping it with a material with stronger ablative response for a given laser energy.

3.7 HIGH-SPEED IMAGING DIAGNOSTICS

In this study, to monitor hypersonic flyers and the flyer-driven shock waves, shadowgraph and schlieren imaging technique is used. The Fig 3.12 schematic presents only the schlieren technique which can be easily modified to shadowgraph by removing the knife edge from the optical path. Both the Schlieren and Shadowgraph techniques involve intense backlight, an infinity corrected objective trained at the flyer trajectory, followed by a tube lens to collimate the image passed into a high-speed camera to capture the event. A knife edge in addition is used to improve the image contrast and enable flow visualization around the flyer.

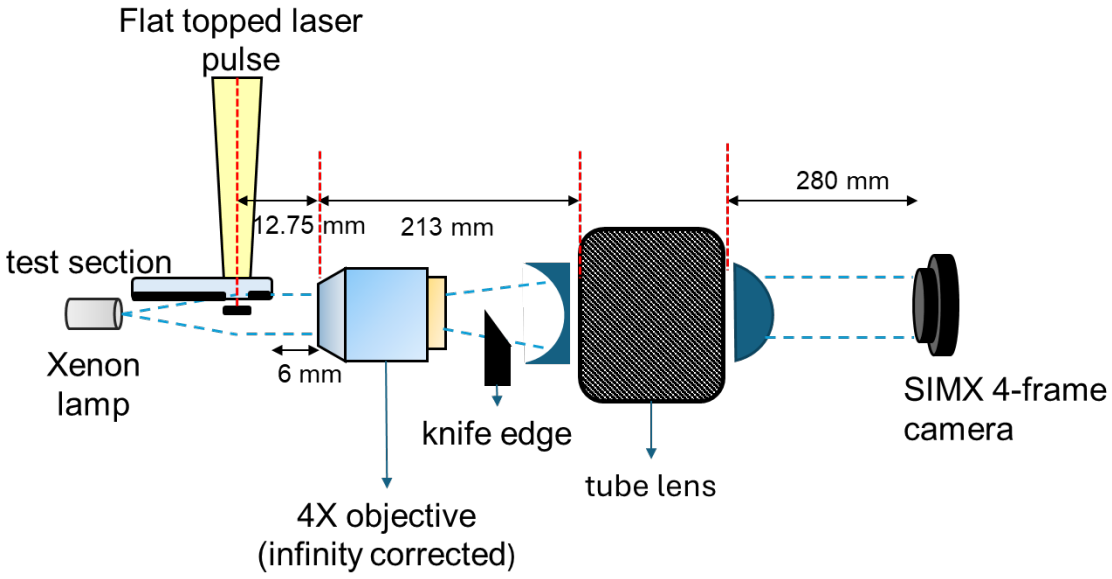

Fig 3.12. Top view of the schematic diagram of schlieren imaging setup composing a light source, a test section to launch the flyer, a 4X objective, a knife edge, tube lens of 200 mm focal length and a 4 channel SIMX high-speed camera. The perspective of this schematic is such that the blue circle in the test section represents thew flyer which is launched towards the viewer, so that the camera is trained on the flyer and flyer-driven shock profile.

Considering the size and speed of the flyer launched in this study the described imaging components (shown in Fig 3.12) are chosen. First, as the flyer launched in this study is at a speed of 2 to 4 km/s, the exposure time to capture the event needs to be in nano seconds. For an event with nano seconds exposure time, xenon-lamp (PX-2 from ocean insights) as a light source is ideal, (Refer Fig 3.12) which offers high-intensity light with a pulse duration of 5 μs. Second, to magnify the flyer of diameter 500 μm during the event, a 4X infinity corrected objective (0.13 N.A. 4X objective from OLYMPUS UPlanFLN) with a tube lens of focal length +200 mm is used. The distance between the infinity-corrected objective and the tube lens is 213 mm. This distance is optimal for the light passing through the tube lens to be collimated, as shown in Fig 3.12. This collimated light is passed through a high resolution intensified-CMOS 4 channel camera (SIMX4 from Specialised-Imaging) in which exposure time can be set to minimum of 3 ns in each channel. Finally, to capture the shock wave driven by the flyer and the flow behind it, a knife edge is used at the focal plane of the objective, as shown in Fig 3.12.

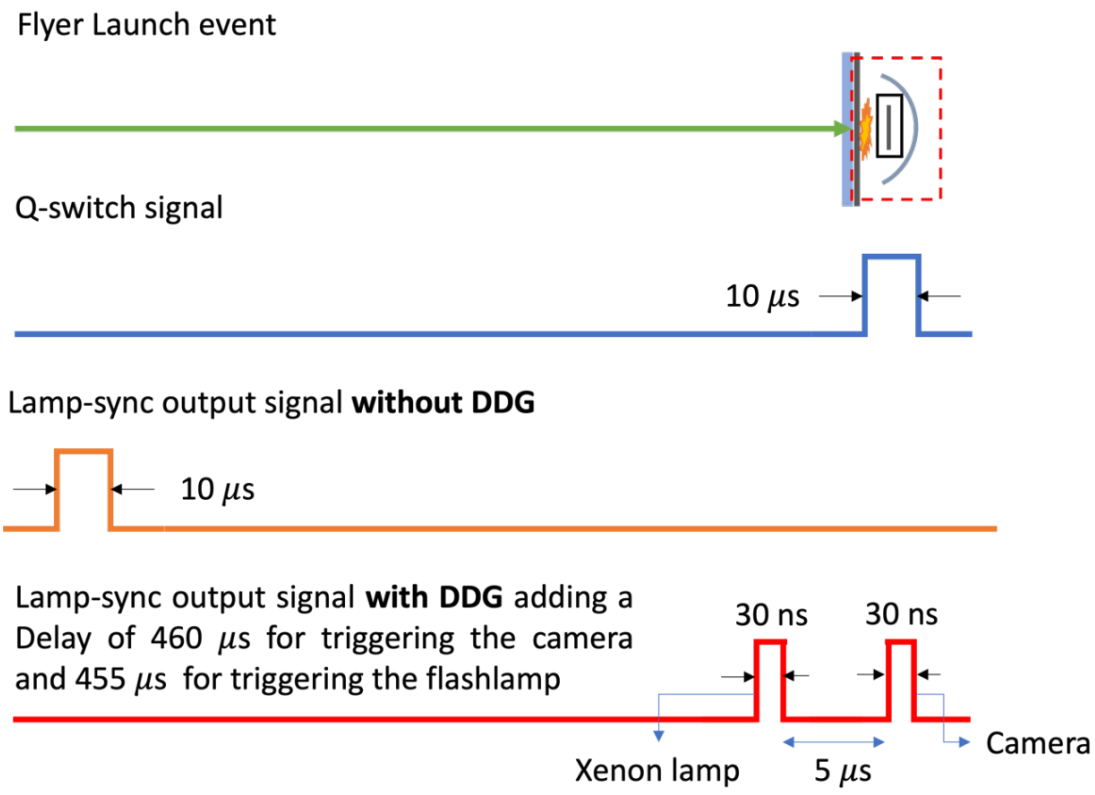

Fig 3.13. Pulse diagram of Q-switch signal and lamp-sync out signal with and without DDG (Digital Delay Generator), and showing the synchronization of the flyer launch event with the camera and xenon lamp

To follow the flyer-launch event, synchronization of the launch event with the camera and the light source is crucial. Fig 3.13 presents the various phenomena useful for synchronization on a time scale to aid subsequent discussion. To trigger the camera and the xenon lamp, two output signals from the laser power unit can be used, namely, Q-switch and lamp-sync out, in which the Q-switch signal is the closest to the flyer launch event only with nano seconds delay (Q-switch signal is the 'blue pulse' shown in Fig 3.13). However, the Q-switch signal is not ideal for synchronization, since, in this case, the light source needs to be triggered 5 microseconds earlier than the camera. Hence, the alternative is to use the output signal from the lamp-sync out. The lamp-sync out ('orange pulse' in Fig 3.13) gives out a pulse 460 μs prior to the launch event (see Laser section to understand delay between flash lamps and Q-switching). To delay the pulse by 460 μs such

that the lamp-sync out signal is in sync with the flyer launch event, a DDG (Digital Delay generator) is used. In this, first, the DDG is externally triggered by the lamp-sync out signal and a delay of 460 μs is fed to one of the channels in the DDG through which the camera is triggered ('red pulse' labelled 'camera' in Fig 3.12) and 455 μs to the channel through which the flash lamp is triggered ('red pulse' labelled 'xenon lamp' in Fig 3.13). Through this delay feed in the DDG channels, both the camera and the xenon flash lamp get triggered such that the instance of laser pulse ablating the epoxy glue can be captured as our temporal reference point (i.e.), the instance we take t = 0. Using this setup, the flyer launch event both with and without the light source can be captured and the experimental data collected will be presented and discussed in detail in the next section.

3.8 REFERENCES

[1] Brown. K. E., Shaw. W. L., Zheng. X., and Dlott. D., "Simplified laser-driven flyer plates for shock compression science," *Review of Scientific Experiments*, Vol. 83, No. 10, 2012 Doi: 10.1063/1.4754717

[2] Swift. D.C., Niemczura. J. G., Paisley. D. L., Johnson. R. P., Luo. S., and Tierney T. E., "Laser launched flyer plates for shock physics experiments," *Review of Scientific Instruments*, Vol. 76, 2005

[3] Fry. M. B. and Gonthier. K. A., "A simplified model for ballistic initiation of thin energetic targets by micro-flier impact," *International Journal of Mechanical Sciences*, Vol. 84, 2014

[4] K. Ito., T. Aizawa., and D. L. Paisley., "Laser-driven shock device for real-time Hugonoit measurement," *Rev. High Pressure Sci. Technol,* Vol. 7, 1998

[5] Shaw. W. L, "Reactive solids under shock compression," PhD dissertation, Department of Chemistry, University of Illinois Urbana-Champaign, Illinois, 2016

[6] S. Watson and J. E. Field, Integrity of thin laser-driven flyer plates, *J. Appl. Phys.* Vol. 88, 2000

CHAPTER 4: IMAGING SHOCK WAVE FORMATION IN SUPERSONIC/HYPERSONIC LASER LAUNCHED FLYERS

This section features data obtained from the new benchtop Nd: Glass laser-driven flyer plate and diagnostic tools built during the course of this work as detailed in Chapter 3. With this setup, there is an unprecedented opportunity to study the flow physics of supersonic/hypersonic vehicles previously explored largely through simulations and modelling work. The convenience inherent in tabletop experimentation allows us to expand the range of shock wave measurements. Multiple experiments with flyers of various dimensions (and other projectiles in future) can be launched up to a speed of 5 km/s in both vacuum and gaseous environment, thus expanding fundamental understanding of shock wave formation and its shape factors, shock standoff distance, and plasma formation among others.

4.1 HIGH-SPEED IMAGING TO TRACK EMISSIONS

In the current study, to drive shock waves in gaseous media and simulate high-speed phenomena, aluminum (Al-1101) flyers of thickness 25 μm and diameter 500 μm are punched out at STP conditions in air. The imaging was performed using the instrumentation and diagnostics detailed in chapter 3 using both dark field imaging (representative images in Fig 4.1) as well as back-lit shadowgraph and schlieren imaging (as shown in Fig 4.2). The images acquired in this fashion capture the profile of the flyer in various stages of its flight based on the delay settings used and the window of observation

To punch out a flyer, a laser pulse with desired energy is focused onto the aluminum foil plated on a glass substrate adhered by a thin epoxy layer. The preparation of the metal foil epoxied to the glass substrate can be found in reference [ref]. The laser energy is partially absorbed by the epoxy

at the interface to produce a hot plasma whose temperature can rise to thousands of kelvins. The formation and rapid expansion of the plasma can be followed using dark-field imaging shown in Fig 4.1. The plasma expansion spans a significantly long period (in this case over 580 ns) likely contributing to the initial accelerating of flyer after spalling of the flyer from the foil adhered to the glass substrate.

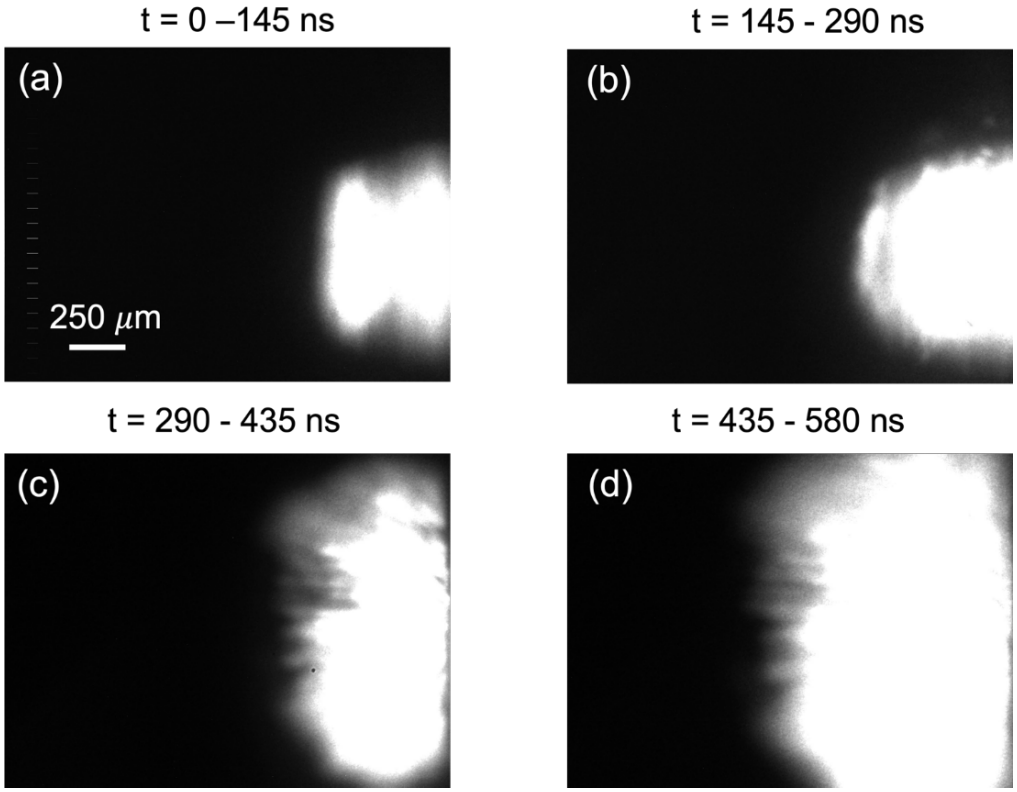

Fig 4.1. High-speed images of laser-induced plasma formation for a pulse energy of 1000 mJ. The images were captured contiguously using a 4X objective with an exposure time of 145 ns. The scale of 250 μm applies to all the images in this figure. The observation period 't' is mentioned above the images

Dark field imaging provides additonal advantages other than just following initial spallation of the flyer, that includes probing the formation of flow compressed plasma expected in shockfronts ahead of hypersonic projectiles. These imaging can be elevated into hyperspectral imaging to acquire temperature maps and operated along with spectroscopy to identify chemical species in plasma.

4.2 BACKLIT IMAGING TO CHARACTERIZE SHOCK WAVES FORMED BY LASER-LAUNCHED FLYERS

The disruption of air by the flyer during the supersonic/hypersonic flight is complex. This section aims to illustrate the evolution of complex flow fields around the flyer through high-speed imaging techniques.

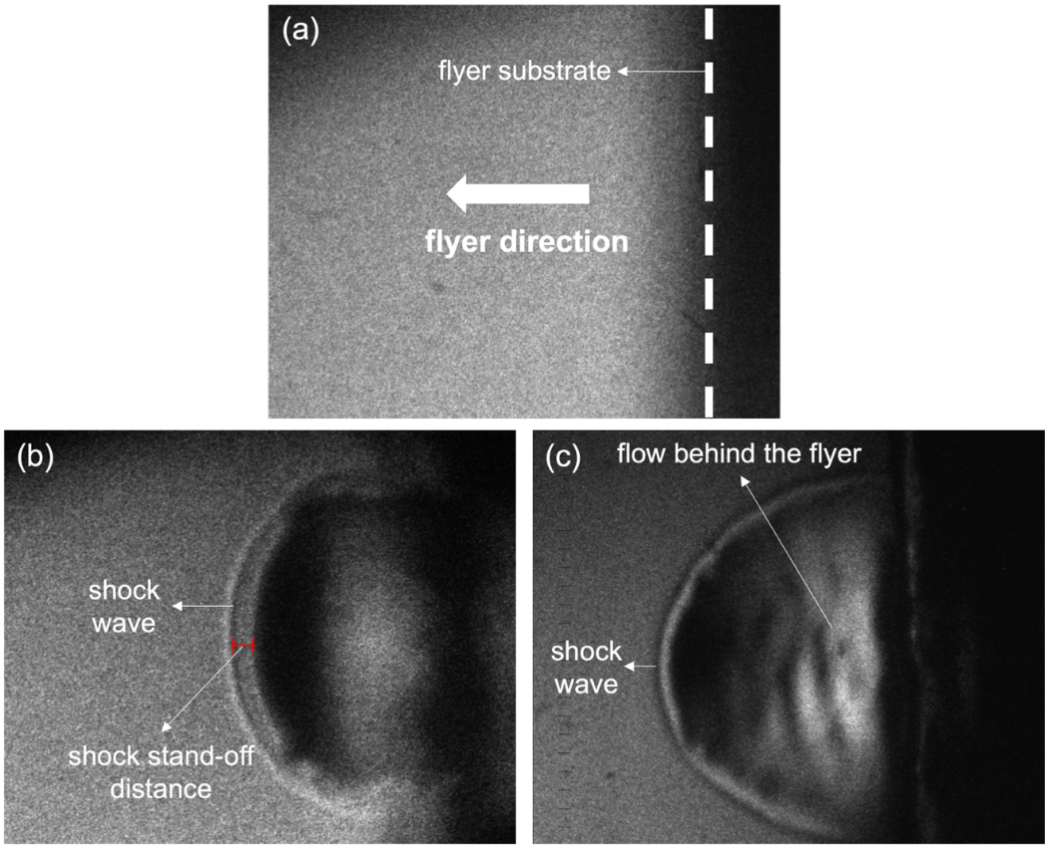

Fig 4.2. (a) Representative image of the field of view prior to the launch with the flyer substrate to the extreme right such that we expect the flyer to travel from right to left. (b) Typical shadowgraph captured with a 4X objective and (c) schlieren image captured with a 2.5X objective. (b) and (c) images were acquired using 5 ns exposure to image the shock-front generated by a flyer travelling at 1 km/s.

A typical profile image of the flyer substrate within the field of view of the high-speed camera backlit using a suitably synchronized flashlamp, prior to the flyer launch is presented in Fig 4.2a. The figure shows the direction of the flyer launch (indicated with an arrow labelled ‘flyer direction’

in Fig 4.2a) when the laser hits the flyer substrate from the right (with the substrate edge being represented as white dash line).

As an example of the back-lit imaging capabilities built, single images of the flyer captured using shadowgraph and schlieren imaging technique, are shown in Fig 4.2b and 4.2c. The orientation of both the images is the same as shown in Fig 4.2a with flyer and associated shock front's path extending from right to left.

The projection of line-of-sight information onto the focal plane of high-speed camera through both these optical systems, it is possible to qualitatively resolve the 2 D phenomena of the flyer and the flow-field feature, namely the shock wave, and the shock standoff distance between the edge of the flyer and the shock wave. These features are marked in the images Fig 4.2b and 4.2c.

However, the shadowgraph technique does not offer optical image of the flyer; it is a shadow projecting the salient features of the flyer, namely, the flyer-driven shock wave and the dark region behind it comprises of the opaque flyer and other optically dense flow features and spallation of micro debris as shown in Fig 4.2b. To capture the weak flow disturbances apart from the shock wave, such as the turbulence imaged in exaggerated detail (shown in Fig 4.2c), schlieren technique is used due to its high-sensitivity and the ability to capture the variation in illumination. The crucial difference in both imaging techniques is using a vertical knife-edge at the focal plane of the 2.5x objective as shown in Fig 3.12 in chapter 3.

It is pertinent to note that in the current study, both the techniques are unable to resolve the flyer due to the limited illumination intensity of the xenon flash lamp employed to backlight the field-of-view in the imaging diagnostics. To capture the phase difference in this case, a high-intensity light source like a laser would be advantageous.

For the present preliminary study, only the data collected from shadowgraph technique is used and additional imaging acquired by implementing schlieren technique can be pursued in future.

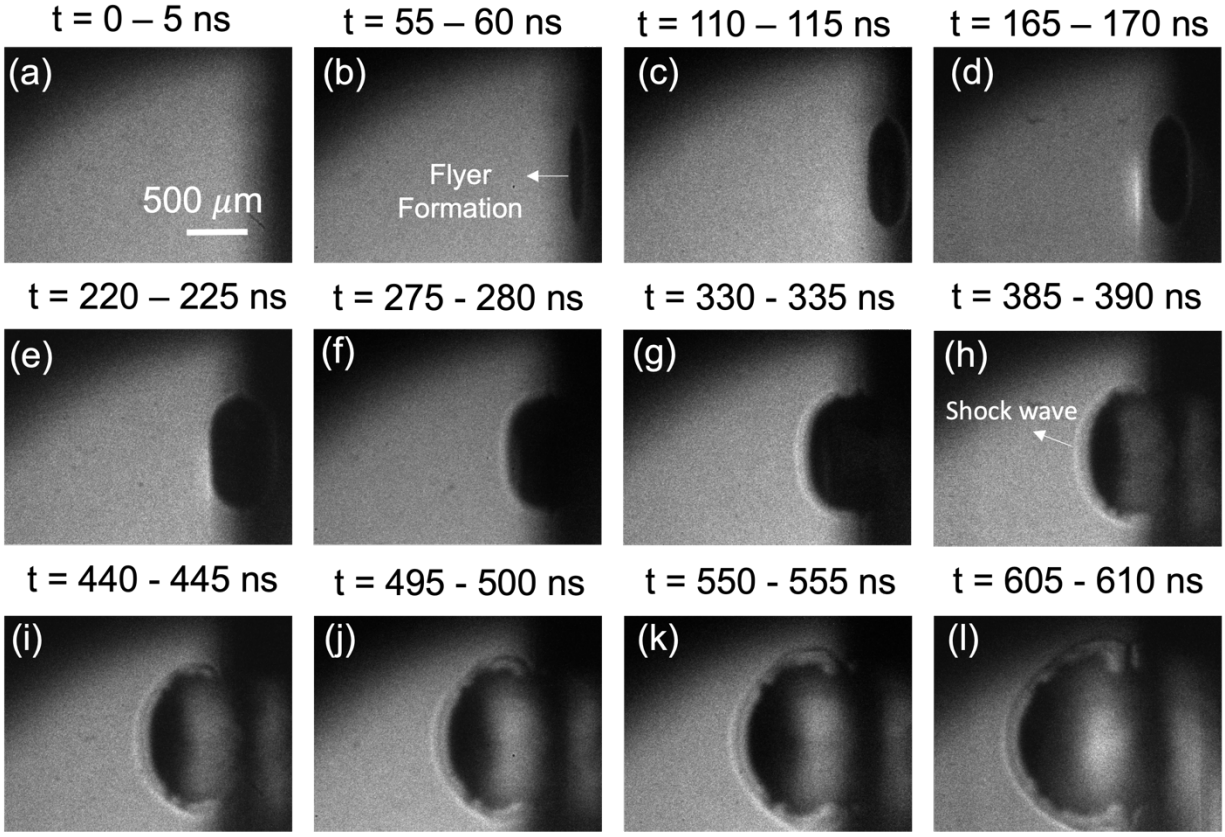

Fig 4.3. Representative shadowgraphs showing formation of flyer and the flyer-driven shock wave for a laser energy of 500 mJ with an exposure time of 5 ns and an interframe of 50 ns. The scale of 500 μm applies to all the images in this figure. The observation period 't' is mentioned above the images

To study the flyer behavior in terms of velocity and planarity, and development of the shock wave during its flight, the initial exploration using shadowgraph imaging was found to be sufficient. Fig 4.3 presents a sequence of shadowgraphs captured from the early launching of 25 μm thick aluminum flyer at STP conditions using a laser pulse of 500 mJ up to several hundred nanoseconds into its flight. Each frame captured has an exposure of 5ns and acquires a representative image of the shock front at various stages of flyer flight by repeat experimentation with different delay settings as the high-speed camera used, SIMX-4 is only capable of capturing 4 frames at a time.

From Fig 4.3 it is clear that initial spallation of the flyer from the metal foil shows a flat-topped region elevating from the flyer substrate (as seen in Fig 4.3 b-f) and slowly changes to a more bow shaped front, aligning with the formation of the first discernable shockwave ahead of it as evidenced in image Fig 4.3h. The development of bow-shaped front of the flyer in Fig 4.3h could be because of the pressure difference in the flow-field around the flyer, as discussed in Chapter 1 (section 1.2). Further, the shape of the shock progressively becomes pronouncedly curved as the flyer flies by with the shock standoff distance observably increasing as evidenced from Fig 4.3i to 4.3l. Through these images, flyer distance from the substrate, and shock stand-off distance between the edge of the flyer and the shock wave can be acquired as previously discussed using the features highlighted in Fig 4.2 and 4.3.

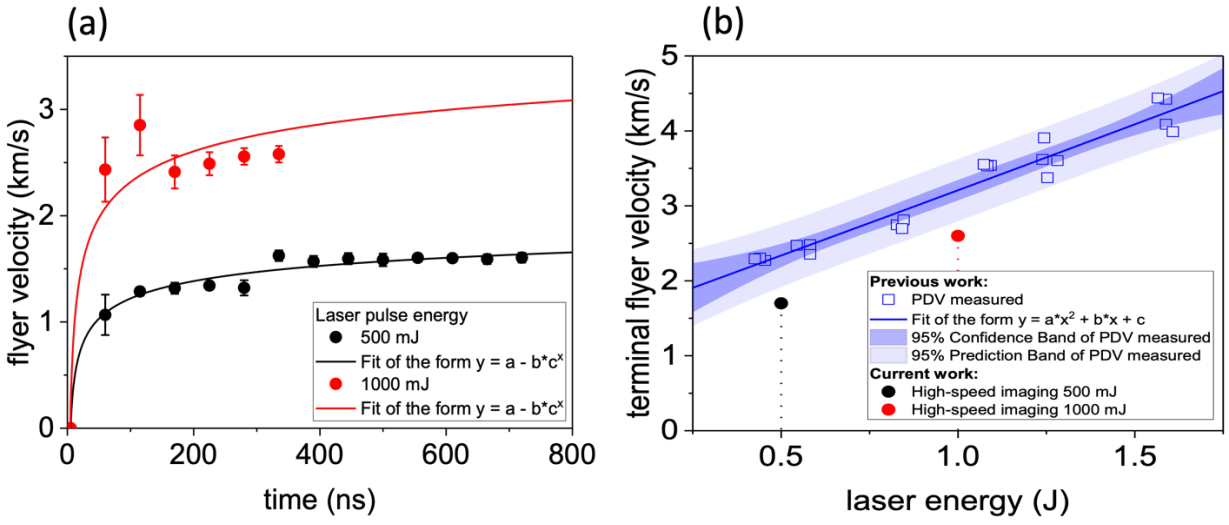

Fig 4.4. (a) Flyer velocities of 25 µm thick aluminum flyers measured using high-speed imaging launched using pulse energies of 500 mJ and 1000 mJ along with (b) the terminal velocities of flyers in this work compared to previous work on similar dimension flyer's terminal velocities measured using PDV over a range of laser energy used to launch them. Each point in Fig 4.4a represents the average of at least 10 repeat experiments while the error bars show the range of one standard deviation.

Based on the distance the shock front and the flyer travels between successive frames, the flyer velocity can be estimated. Fig 4.4a shows the evolving flyer velocities estimated from

shadowgraphs presented as a function of time (refer to Fig 4.3) for flyers launched at two laser energies. The solid lines are fits to help draw the eye to observe the trends in discrete experimental data obtained. Flyers launched at both energies show strong initial acceleration before they attain their terminal velocities.

Previously collected terminal velocities for same thickness aluminum flyers launched at various pulse energies in the same setup along with the terminal velocities of the horizontally launched flyers estimated using high-speed imaging in this work are presented in Fig 4.4b. The maximum flyer velocity acquired from the shadowgraph images for a laser energy of 500 mJ and 1000 mJ (shown in Fig 4.4a) are in close proximity to the 95% prediction band of the terminal velocities measured using PDV as shown in Fig 4.4b.

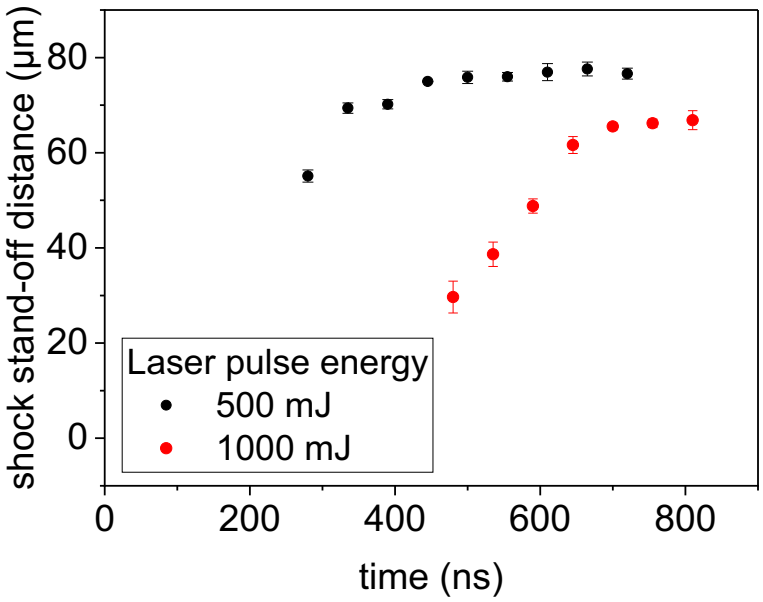

Fig 4.5. Shock stand-off distance of a 25 μm thick flyer driven by a laser energy of 500 mJ and 1000 mJ. Each point is an average of at least 10 repeat experiments and the error bars represent one standard deviation.

The shock stand-off distance acquired from each frame from the instance of laser pulse interaction with flyer substrate (t=0) is obtained and plotted as a function of time for flyers generated by pulses at two energies 500 mJ and 1000mJ in Fig 4.5. The lack of standoff distance in initial frames is

due to the fact that early time slow flyers do not exhibit any shock or have no discernable features attributable to a shock front. For flyers launched at both energies, the shock standoff distance grows until it reaches a plateau with the flyer launched at the higher energy showing a smaller standoff distance of 63 μm as compared to 75 μm for 500mJ launched flyers.

4.3 SUMMARY OF PRELIMNARY INVESTIGATION

The instrumentation built was able to punch out metal flyers of 500 μm diameter with tunable terminal velocities similar to the previous experimental setups. The synchronized imaging tools are capable of tracking all the stages of flyer formation and the evolution of flyer caused shock front. The imaging techniques presented allow for the characterization of various features of the shock front using shadowgraph and schlieren imaging.

Preliminary work showcasing the imaging capabilities shows the development of the bow shaped shock front ahead of an accelerating flyer. The estimated flyer velocities from the shadowgraphs present an estimated velocity difference of 1 km/s between the flyers launched at the two laser energies tested in this work. The inferred terminal velocity values are in reasonable agreement with previous work that measured flyer velocities using PDV.

The shock standoff distance inferred from the shadowgraphs show the reduction in the standoff distance with increasing flyer terminal velocities. This suggests a threshold at higher flyer velocities where the stand-off distance approaches zero and we observe the formation of a plasma in the shock front due to compression of gases in front of a hypersonic plate.

4.4 FUTURE WORK USING EXPERIMENTAL CAPABILITIES DEVELOPED

Several fundamental aspects of hypersonic flight such as shock front formation, stability of shock front, shock stand-off distance and threshold for formation of plasma can be tracked using the

instrumentation and diagnostic tools developed in this work for a variety of projectiles in different atmospheres.

Based on the preliminary work presented in this chapter, pursuing fundamental science questions such as the threshold for plasma formation in shock fronts and identifying projectile velocity and shape factor's role in shock stability, change in flow fields and plasma formation is achievable using schlieren imaging.

Further, a more application-oriented design of experiment is also possible with this instrumentation. For example, the study of high-speed impacts involving debris such as micro-meteoroids and dust particles with vehicles and space stations for the development shielding materials is also possible. Based on the present study; spallation of the test target, the size of the debris and its velocity over time can be followed using the shadowgraph technique itself. The shadowgraphs presented in Fig 4.6 evidence the nanoseconds resolution capability using a test case of metal and glass debris flying from a test substrate. The debris ejected in these images are glass pieces that are flying < 0.3 km/s (based on the displacement of shards between the two images Fig 4.6a and 4.6b), an order of magnitude lower than the velocity of the flyer (Refer to Fig 4.6).

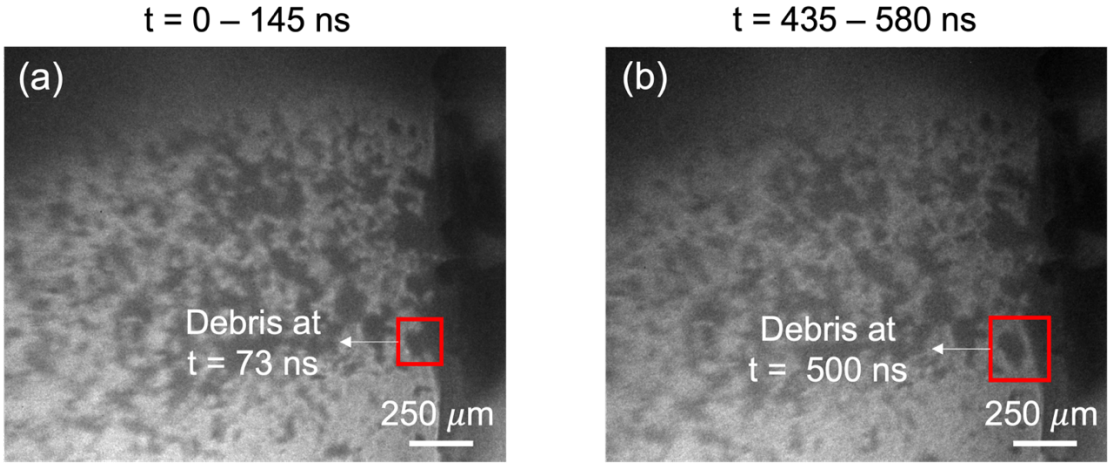

Fig 4.6. Images of debris flying off a glass substrate to showcase the resolution capability of shadowgraph employed in this work. A red box is drawn around a debris in both frames to track its trajectory.

The future work focuses on impacting different targets of a variety of material compositions to visualize the collision phenomena itself including the imaging of damaged region, and the formation and expansion of debris cloud generated by the target during the impact. All aspects of the process can be quantified and used to develop theories and experimental approaches.

Additionally, this instrumentation is used to understand the mechanisms at play between shock – fuel droplet interactions in rotating detonation engines. By adding a suitable droplet generator to the setup and dripping desired sized droplets in the path of customized shocks we can study complex interactions of shock and liquid droplets.

This instrumental and imaging design can unlock several high-throughput benchtop experimentations to help material development and prototyping, hasten application oriented preliminary testing as well as verify and broaden understanding of fundamental scientific concepts in hypersonic research.